

Synthesis, Characteristics, and Applications of Intrinsically Light-Emitting Polymer Nanostructures

Young Ki Hong, Dong Hyuk Park, Seok Ho Lee, and Jinsoo Joo

Abstract Light-emitting π -conjugated polymers and their nanostructures have been intensively studied from the viewpoints of both fundamental research and optoelectronic applications. The characteristics of light-emitting polymer nanostructures, such as light absorption and emission efficiencies, can be tuned through chemical processing and by varying their physical dimensions. In this review article, recent progress in the synthesis, characterization, modification, and applications of light-emitting polymer-based nanostructures is presented. Various synthetic methods for light-emitting polymer nanostructures are introduced, and their intrinsic optical properties at a nanoscale level are summarized. Post-synthetic treatments for modification of the characteristics related to the morphologies and doping states are discussed. Finally, potential applications of these nanostructures to barcode/quasi-superlattice nanowires, biosensors, and nano-optoelectronics are presented.

Keywords π -Conjugation · Barcode · Biosensor · Doping · Electron beam · Hybridization · Hydrothermal · Light-emitting polymer · Nanoscale optical property · Nanostructure · Optoelectronics

Contents

1	Introduction	203
2	Synthetic Methods for Nanostructures	203
2.1	Electrochemical Polymerization	204
2.2	Reprecipitation	206
2.3	Electrospinning	207

3	Optical Properties of As-Prepared Nanostructures	209
3.1	Electrochemically Synthesized Nanotubes and Nanowires	209
3.2	Nanoparticles Prepared by Reprecipitation	214
3.3	Electrospun Nanowires	214
4	Post-synthetic Treatments for Modification of Nanostructure Characteristics	215
4.1	Electrochemical Doping and Dedoping: Cyclic Voltammetry	216
4.2	Unfocused E-Beam Treatment	219
4.3	Hydrothermal Treatment	221
4.4	Hybridization with Metal Nanostructures	222
5	Applications	227
5.1	Barcodes	227
5.2	Focused E-Beam Treatment: Fine Barcodes and Quasi-superlattice	231
5.3	Biosensing	233
5.4	Nano-optoelectronics	236
6	Conclusions and Outlooks	240
	References	240

Abbreviations

1D	One-dimensional
2D	Two-dimensional
3D	Three-dimensional
c-AFM	Conducting atomic force microscope
CCD	Charge-coupled device
CV	Cyclic voltammetry
DBSA	Dodecylbenzenesulfonic acid
E-beam	Electron-beam
HDL	Hybrid double-layered
HR	High-resolution
<i>I</i> - <i>V</i>	Current-voltage
LCM	Laser confocal microscope
LECB	Light-emitting color barcode
MEH-PPV	Poly[2-methoxy-5-(2'-ethylhexyloxy)- <i>p</i> -phenylenevinylene]
NP	Nanoparticle
NT	Nanotube
NW	Nanowire
P3BT	Poly(3-butylthiophene)
P3HT	Poly(3-hexylthiophene)
P3MT	Poly(3-methylthiophene)
PCBM	[6,6]-Phenyl C ₆₁ -butyric acid methyl ester
PEDOT	Poly(3,4-ethylenedioxythiophene)
PL	Photoluminescence
PTh	Polythiophene
SEM	Scanning electron microscope
SPR	Surface plasmon resonance
TEM	Transmission electron microscope
UV-vis	Ultraviolet-visible

1 Introduction

Light-emitting polymers with a π -conjugated structure have attracted considerable interest in the fields of both fundamental science and applied research owing to their fascinating one-dimensional (1D) characteristics and potential optoelectronic applications [1–6]. Figure 1 shows the chemical structures of a few examples of π -conjugated light-emitting polymers: polythiophene (PTh), poly(3-alkylthiophene) (P3AT), poly(3,4-ethylenedioxythiophene) (PEDOT), poly(*p*-phenylenevinylene) (PPV), and poly[2-methoxy-5-(2'-ethylhexyloxy)-*p*-phenylenevinylene] (MEH-PPV).

The π -conjugated structure of light-emitting polymers refers to the alternation of single and double covalent bonds between adjacent carbon atoms [7]. This π -conjugation leads to delocalized π -electrons along the polymeric main chains, which play an important role in the electronic and optical properties of light-emitting polymers [8]. The electronic structures of π -conjugated polymers are successfully described by the Su–Schrieffer–Heeger (SSH) Hamiltonian model [9–11]. As a consequence of the π -conjugated structure, these light-emitting polymers have a semiconducting band gap. Both theoretical and experimental studies have been conducted on chemical processes for engineering the energy band structure of π -conjugated polymers [10, 12–24]. Thus, the optical and electrical properties of π -conjugated polymers can be varied by controlling the energy band structure and by chemical doping.

With rapid developments in nanoscience and nanotechnology, various nanostructures, including nanotubes (NTs), nanowires (NWs), and nanoparticles (NPs), have been fabricated using light-emitting polymers [4–6]. The intrinsic characteristics of π -conjugated polymer nanostructures can be controlled through the physical dimensions, chemical processes, and post-synthetic treatments.

This review article introduces and summarizes the fabrication, characterization, and modification processes as well as optoelectronic applications of various light-emitting polymer nanostructures.

2 Synthetic Methods for Nanostructures

π -Conjugated light-emitting polymer nanostructures, including NTs, NWs, and NPs have been synthesized using template and template-free methods [5, 6, 25–29]. Recently, Jenekhe et al. reviewed various synthetic methods for 1D nanostructures of π -conjugated molecular systems [30]. Template-based methods are categorized into two sub-categories depending on the type of template, i.e., soft templates and hard templates. Anodic aluminum oxide (Al_2O_3), particle track-etched membrane, mesoporous silica, microchannel array, and zeolite are typically employed as hard templates. The synthesis of π -conjugated polymer NTs or NWs with hard templates involves a combination of electrochemical [25, 31–33], chemical [34–37], and organic vapor deposition [38] techniques. The formation of NTs or NWs and their physical dimensions, such as diameter and length, are determined by the

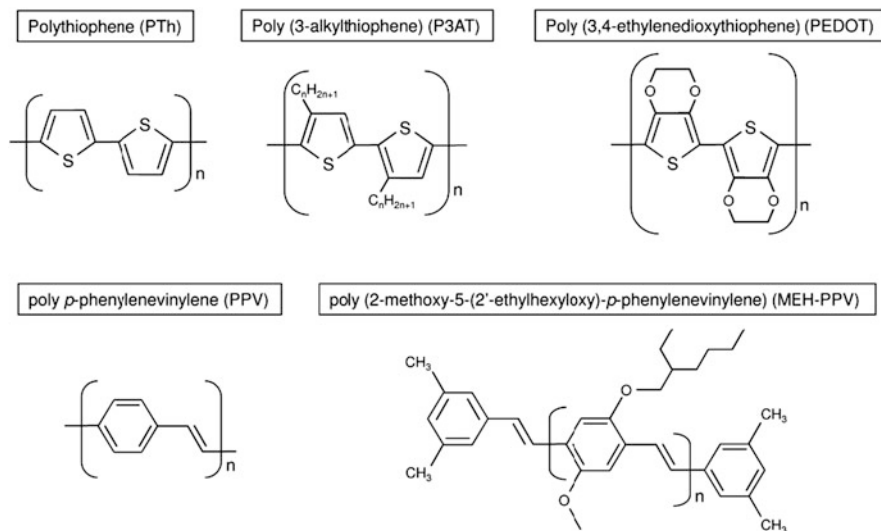


Fig. 1 Chemical structures of various light-emitting polymers with π -conjugated structure

size of the nanoporous template used. Of the template-free methods, this section presents the reprecipitation method for the synthesis of NPs and the electrospinning method for NWs.

2.1 Electrochemical Polymerization

In this section, we focus on the synthesis of light-emitting polymer NTs and NWs through electrochemical polymerization using nanoporous Al_2O_3 templates. For electrochemical synthesis of the polymer NTs and NWs, the electrolyte consists of a solution of monomers and dopants in appropriate solvents such as deionized water, *N*-methyl-2-pyrrolidinone (NMP), and acetonitrile (CH_3CN). Aniline, pyrrole, and thiophene and its derivatives such as 3-methylthiophene (3-MT), 3-butylthiophene (3-BT), 3-hexylthiophene (3-HT), and ethylenedioxythiophene (EDOT) are typical monomers. Dopants can include anionic salts such as BF_4^- , PF_6^- , and ClO_4^- as well as camphorsulfonic acid (CAS) and dodecylbenzenesulfonic acid (DBSA), which also act as surfactants that promote homogeneous dispersion of the hydrophobic monomers in deionized water. Thin metal layers, for example, gold (Au), platinum (Pt), and aluminum (Al), are thermally evaporated on one side of the nanoporous Al_2O_3 template and attached to the metal working electrode.

When a current or voltage is applied to the electrodes, the monomers are oxidized at the surface of the electrode. As a result of the initial oxidation, the monomers form radical cations that react with other monomers in the electrolyte to form oligomeric products, as shown in Fig. 2. The extended π -conjugation in the polymeric chain (i.e., polymerization) is assisted by dopant anions, and the synthesis and doping of the

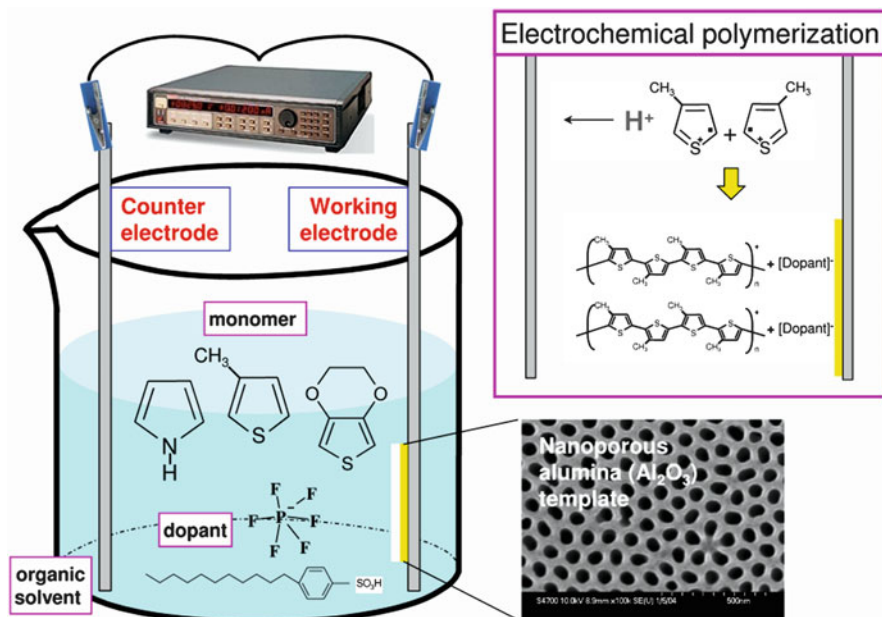


Fig. 2 Electrochemical polymerization method using alumina (Al₂O₃) nanoporous template

light-emitting polymer NTs and/or NWs are generally accomplished simultaneously [39]. After polymerization, an acid (e.g., HF or H₃PO₄), base (e.g., NaOH or KOH), or organic solvent can be used to dissolve the nanoporous template and isolate the synthesized NTs or NWs. The intrinsic optical properties of the electrochemically synthesized light-emitting polymer NTs or NWs can be controlled by the synthetic conditions such as molar ratio of monomer to dopant, applied current or voltage, synthetic temperature, and type of solvent used for the dissolution of the nanoporous template.

Figure 3 shows scanning electron microscope (SEM) and transmission electron microscope (TEM) images of various light-emitting polymer NTs or NWs synthesized through electrochemical polymerization with nanoporous Al₂O₃ templates [40–43]. The SEM image in Fig. 3a shows open ends of the P3MT NTs, and the inset shows filled ends of P3MT NWs. In the TEM image, the formation of NTs can be clearly identified; the thickness of the NT wall was estimated at 5–10 nm. In order to synthesize P3MT NTs, a current density of ~1.7 mA/cm² was applied for 18–20 min. For the formation of P3MT NWs, the applied current density and polymerization time were increased up to 2.0–2.5 mA/cm² and ~23 min, respectively [40]. Martin et al. reported that polymerization was initiated at the bottom of nanopores on the working electrode and proceeded along the inside walls of the nanoporous Al₂O₃ template [44]. The results indicated that NTs could be converted to NWs by increasing the polymerization time and applied current density.

The formation of P3BT NWs can also be controlled by adjusting the applied current density and polymerization time [41]. P3BT NWs with open ends at the top

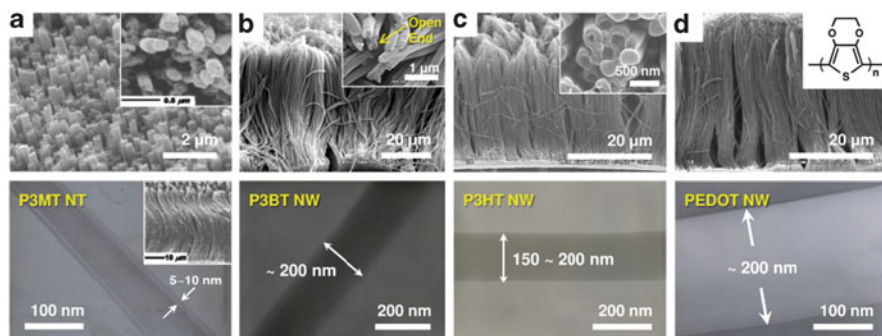


Fig. 3 SEM and TEM images of the electrochemically synthesized light-emitting polymer NTs and NWs: (a) P3MT NTs, (b) P3BT NWs, (c) P3HT NWs, and (d) PEDOT NWs. [Reproduced in part from (a) [40], (b) [41], (c) [42], and (d) [43] with permission. (a) Copyright 2005 American Institute of Physics. (b) Copyright 2008 Electrochemical Society. (c) Copyright 2007 American Institute of Physics. (d) Copyright 2008 Elsevier B.V.]

are observed in the SEM and TEM images in Fig. 3b. The length and diameter of the NWs are $\sim 20 \mu\text{m}$ and $\sim 200 \text{ nm}$, respectively. A TEM image of an isolated single P3HT NW with open ends is shown in Fig. 3c. The diameter of the single P3HT NW is 150–200 nm. Figure 3d shows the SEM and TEM images of PEDOT NWs. A uniform and continuous array of the PEDOT NWs with a length of $\sim 30 \mu\text{m}$ was observed by SEM. From the magnified TEM image, the diameter of a single PEDOT NW can be estimated at $\sim 200 \text{ nm}$.

2.2 Reprecipitation

Horn and Rieger reviewed the various synthetic methods and optical properties of organic NPs [45]. Reprecipitation is a representative method for fabricating π -conjugated polymer NPs [45–48]. As shown in Fig. 4, a polymer powder is dissolved in an amphiphilic solvent (e.g., tetrahydrofuran) and the polymer solution rapidly dropped into deionized water under vigorous stirring. During this process, polymer molecules form spherically shaped NPs through aggregation in order to minimize the interfacial energy between the polymer solution and water. The size of the NPs can be controlled by varying the concentration of the polymer solution, stirring speed, temperature of deionized water, as well as by addition of polar solvents such as acetone. A mini-emulsion method has been recently developed to synthesize homogeneously dispersed polymer NPs [45, 49, 50]. In this method, an aqueous solution of surfactant is added to a solution of the polymer in an organic solvent such as chloroform. The mixture of solutions is then emulsified through ultrasonication to afford an aqueous suspension of polymer NPs.

Figure 5a shows an SEM image of MEH-PPV NPs fabricated by reprecipitation [51]. The NPs were spherical and had diameters estimated to be in the range

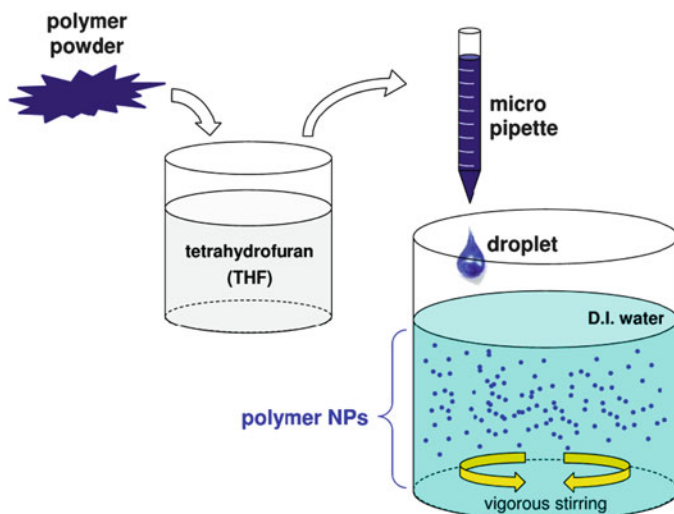


Fig. 4 Scheme showing the reprecipitation process

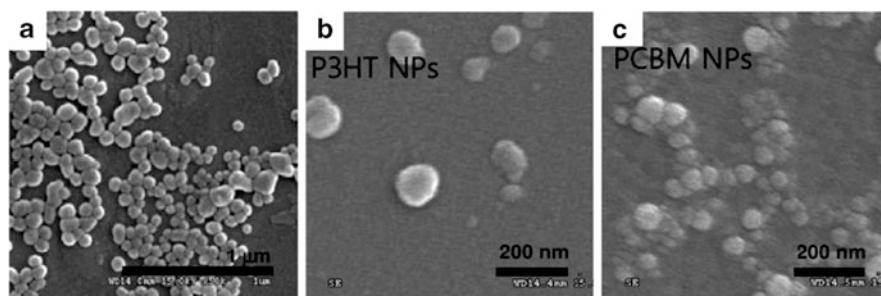


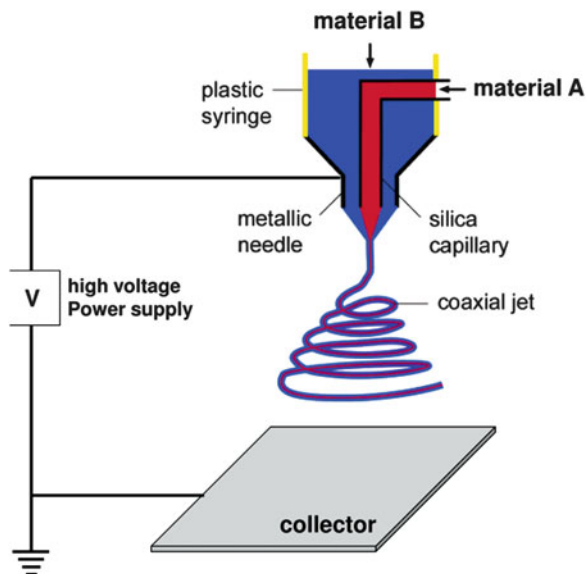
Fig. 5 SEM images of (a) MEH-PPV NPs, (b) P3HT NPs, and (c) PCBM NPs. [Reproduced in part from (a) [51] and (b, c) [52] with permission. (a) Copyright 2009 American Chemical Society. (b, c) Copyright 2012 Royal Society of Chemistry.]

40–150 nm. SEM images of P3HT and [6,6]-phenyl C_{61}^- butyric acid methyl ester (PCBM) NPs fabricated by the mini-emulsion method are shown in Fig. 5b and Fig. 5c, respectively [52]. The diameters of the P3HT and PCBM NPs were $\sim 108 (\pm 28)$ and $77 (\pm 20)$ nm, respectively.

2.3 Electrospinning

Electrospinning is a simple, inexpensive, and efficient method based on application of a high electric field for fabricating relatively long and continuous NWs (i.e., nanofibers) of various organic and/or inorganic materials [53–57]. With this

Fig. 6 Modified electrospinning system with two-capillary spinneret. [Reproduced with permission from [59]. Copyright 2004 American Chemical Society]



method, ultrathin fibers can be obtained from solutions and melts by the uniaxial elongation of viscoelastic jets owing to the electrostatic repulsive interaction between surface charges. Conventional electrospinning systems consist of three major components: a high-voltage power supply, a metallic needle (i.e., capillary spinneret), and a grounded collector as the counter electrode. An electric field applied between the metallic needle and collector (typically on the order of 1×10^5 V/m) causes charging on the surface of a droplet at the needle tip, which transforms into a funnel-shape known as a Taylor cone. Then, a fluidic jet is ejected that is accelerated from the needle tip owing to the electrostatic force from the oppositely charged collector plate [30, 54, 56].

The dimensions and morphology of the electrospun nanofibers are determined by the intrinsic properties of the materials (e.g., chemical structure, molecular weight, and solubility), properties of the solvent (e.g., surface tension, viscosity, conductivity, vapor pressure, polarity, and dielectric constant), and external processing parameters (e.g., electric potential and field distribution, concentration of constituent materials and any additional ions, and feed rate). Electrospinning systems have been modified to allow greater control over the process and to tailor the structure of the nanofibers. The substitution of a rotating drum for a collector plate results in uniform mats of electrospun nanofibers [58]. Figure 6 shows a modified electrospinning system with a two-capillary spinneret for different materials [59]. This system affords composite nanofibers or NTs combined with the proper elimination process of inner materials.

Laforge et al. reported on a combination of electrospinning and vapor-phase polymerization to fabricate PEDOT nanofibers [60]. Figure 7 shows the optical microscope and SEM images of these electrospun PEDOT nanofibers. Their average diameter was $350 (\pm 60)$ nm.

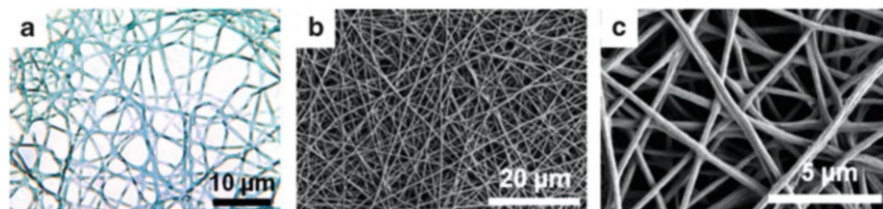


Fig. 7 (a) Optical microscope and (b, c) SEM images of PEDOT nanofibers at different magnifications. [Reproduced with permission from [60]. Copyright 2011 Elsevier B.V.]

3 Optical Properties of As-Prepared Nanostructures

In this section, we discuss the optical properties of the as-prepared light-emitting polymer nanostructures described in Sect. 2. The ultraviolet and visible (UV–vis) absorption and photoluminescence (PL) spectra of the polymer nanostructures dispersed in organic solvents are introduced and discussed. The nanoscale and solid-state optical properties of a single unit of the light-emitting polymer nanostructures can be investigated using high-resolution laser confocal microscope (LCM) systems built around an inverted optical microscope, coupled with luminescence color charge-coupled device (CCD) measurements. In this method, the LCM PL intensities of single units of nanostructures are measured in units of voltage or photon count. For a quantitative comparison of the nanoscale and solid-state optical properties of polymer nanostructures, the LCM PL spectra must be normalized with respect to those of pristine (i.e., as-prepared) samples. The details of the methods for the LCM and CCD experiments are reported elsewhere [41, 42, 61–65].

3.1 Electrochemically Synthesized Nanotubes and Nanowires

3.1.1 P3MT Nanotubes

Park and coworkers reported that the doping level and structural properties of electrochemically synthesized P3MT NTs could be controlled by varying the synthetic temperature [40]. Figure 8a shows a comparison of the UV–vis absorption spectra of P3MT NTs synthesized at various temperatures. For HF-treated P3MT NTs, the π – π^* transition peak shifted from 2.27 to 2.33 eV for NTs synthesized at 20°C and –20°C, respectively. Furthermore, as the synthetic temperature decreased from 20°C to –20°C, the intensity of the bipolaron peaks at ~1.6 eV increased, implying a variation in the degree of doping with temperature [24]. For NaOH-treated P3MT NTs, a bipolaron peak was only observed at ~1.6 eV for the NTs synthesized at –20°C, as shown in the inset of Fig. 8a. The π – π^* transition peak of the NaOH-treated P3MT NTs was observed at ~2.15 eV. The results indicate that the optical properties of P3MT NTs can be controlled by varying the synthetic

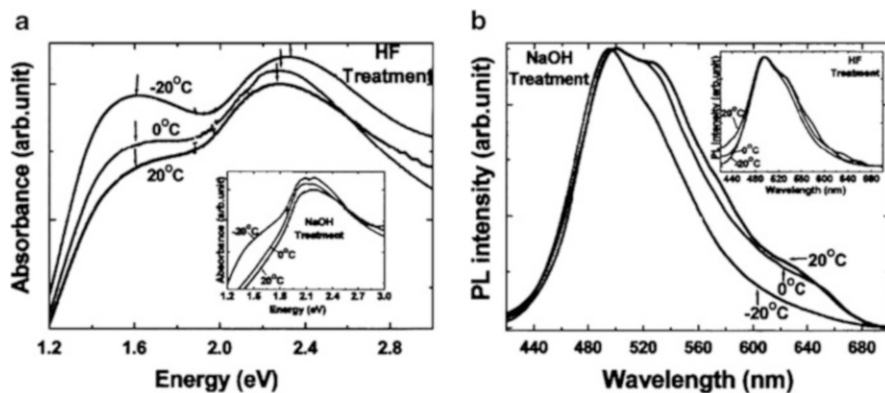


Fig. 8 (a) Comparison of UV–vis absorption spectra of HF-treated P3MT NTs synthesized at -20°C , 0°C , and 20°C . *Inset*: spectra of NaOH-treated P3MT NTs synthesized at -20°C , 0°C , and 20°C . (b) Comparison of solution PL spectra of NaOH-treated P3MT NTs. *Inset*: spectra of HF-treated P3MT NTs. [Reproduced with permission from [40]. Copyright 2005 American Institute of Physics.]

temperature as well as the template-dissolving organic solvents. It was reported that lower temperatures in electrochemical synthesis of conducting polymers lead to enhanced electrical properties owing to the better chain alignment and extended conjugation length [66].

Figure 8b shows the normalized solution PL spectra of P3MT NTs synthesized at 20°C , 0°C , and -20°C . For NaOH-treated P3MT NTs, the main PL peaks were observed at $\sim 490\text{ nm}$, together with shoulder peaks at $\sim 530\text{ nm}$ attributed to the S_0-1 transition. As the synthetic temperature decreased, the shoulder peak at $\sim 530\text{ nm}$ disappeared, and the main peak at $\sim 490\text{ nm}$ became sharper. As shown in the inset of Fig. 8b, similar dependence on the synthetic temperature was observed for HF-treated P3MT NTs. These results might be attributed to the better chain alignment and extended conjugation for the P3MT NTs synthesized at lower temperatures, in agreement with the findings based on the UV–vis absorption spectra.

3.1.2 P3MT Nanowires

Recently, Hong et al. reported the optical properties of electrochemically synthesized P3MT NWs that were separated from nanoporous Al_2O_3 templates by treatment with HF [62]. Figure 9a shows the UV–vis absorption spectrum of P3MT NWs that were synthesized at a lower temperature and higher applied current than those shown in Fig. 8. A broad and relatively intense bipolaron absorption band was observed at $\sim 780\text{ nm}$ and a relatively weak $\pi-\pi^*$ transition peak was observed at $\sim 390\text{ nm}$, which indicates that the P3MT NWs shown in Fig. 9 were more heavily doped than those shown in Fig. 8.

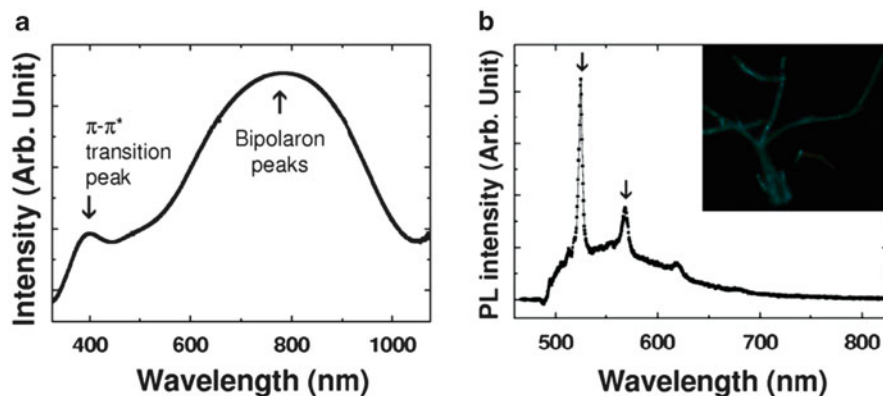


Fig. 9 (a) UV-vis absorption spectrum of as-prepared P3MT NWs. (b) LCM PL spectrum of single P3MT NW. *Inset*: color CCD image of single P3MT NW. [Reprinted with permission from [62]. Copyright 2011 Wiley-VCH.]

Figure 9b shows the LCM PL spectrum of an isolated single P3MT NW. The sharp peaks observed at 525 and 569 nm are the anti-Stokes' Raman shift of the P3MT material corresponding to 1,459 and 2,917 cm^{-1} , which were assigned to the symmetric $\text{C}_\alpha=\text{C}_\beta$ ring-stretching mode and the methyl (CH_3) symmetric stretching mode in the thiophene ring out-of-plane deformation, respectively [63, 67–69]. Excluding these Raman modes, which are commonly observed in nanoscale and solid-state PL measurements, the maximum LCM PL peak was observed at 520–530 nm. This is reflected in the green light emission seen in the color CCD image of the P3MT NWs shown in the inset of Fig. 9b.

3.1.3 P3BT Nanowires

Park et al. also reported that the doping levels of electrochemically synthesized P3BT NWs are correlated with the type of solvent (i.e., acid or base) used for dissolution of the nanoporous Al_2O_3 templates [41]. Figure 10a shows the normalized UV-vis absorption spectra of P3BT NWs. The $\pi-\pi^*$ transition peaks of the P3BT NWs treated with HF and NaOH solutions appeared at 393 and 438 nm, respectively. Thus, the $\pi-\pi^*$ transition peak of the HF-treated P3BT NWs was blue-shifted by ~45 nm compared with that of the NaOH-treated NWs [70]. A broad bipolaron peak was observed at ~816 nm for the HF-treated P3BT NWs; however, this peak almost disappeared in the spectra of the NaOH-treated NWs [71, 72]. These results stem from the light doping and dedoping of the P3BT NWs during treatment with HF and NaOH solutions, respectively.

Figure 10b shows the normalized solution PL spectra of P3BT NWs treated with HF and NaOH solutions. The main PL peaks of the HF- and NaOH-treated P3BT NWs were observed at 547 and 564 nm, respectively. The inset of Fig. 10b shows photographs of light emission from HF- and NaOH-treated P3BT NWs that were

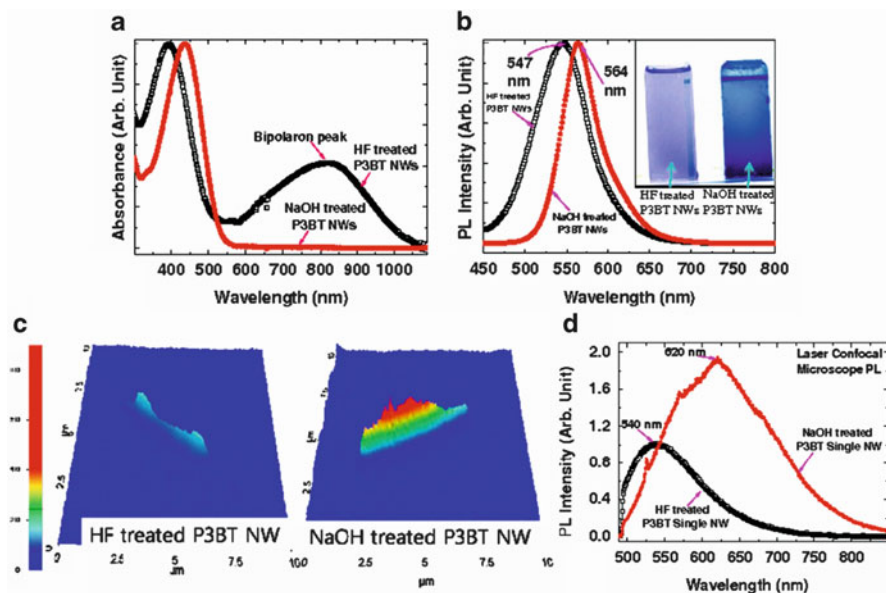


Fig. 10 (a) Normalized UV-vis absorption spectra of HF- and NaOH-treated P3BT NWs. (b) Normalized solution PL spectra of corresponding samples. *Inset*: luminescent photographs of HF- and NaOH-treated P3BT NWs. (c) 3D LCM PL images of isolated single NWs. Color scale bar represents LCM PL intensities in the unit of measured voltages. (d) Comparison of LCM PL spectra of HF- and NaOH-treated P3BT NWs. [Reprinted with permission from [41]. Copyright 2008 Electrochemical Society.]

homogeneously dispersed in chloroform (CHCl_3) solutions. The HF- and NaOH-treated P3BT NWs emitted green and yellow light, respectively.

Figure 10c shows three-dimensional (3D) LCM PL images of isolated single HF- and NaOH-treated P3BT NWs. The LCM PL intensities of the HF- and NaOH-treated P3BT single NWs were 20–25 and 45–55 mV, respectively. The LCM PL intensity of the NaOH-treated P3BT single NW was 1.8–2.8 times higher than that of the HF-treated NW because of the reduction in PL quenching owing to the dedoping effect. Figure 10d compares the averaged LCM PL spectra of isolated single HF- and NaOH-treated P3BT NWs for five different positions on the same NW under the same LCM experimental conditions. The maximum LCM PL peaks of the HF- and NaOH-treated P3BT single NWs were observed at ~540 nm (green–yellow light emission) and ~620 nm (orange–red light emission), respectively. The intensity of the LCM PL peak at 620 nm for the NaOH-treated P3BT NW was about two times higher than that of the HF-treated P3BT NW. The enhanced PL intensity and bright light emission in the NaOH-treated P3BT single NW are attributed to the dedoping effect.

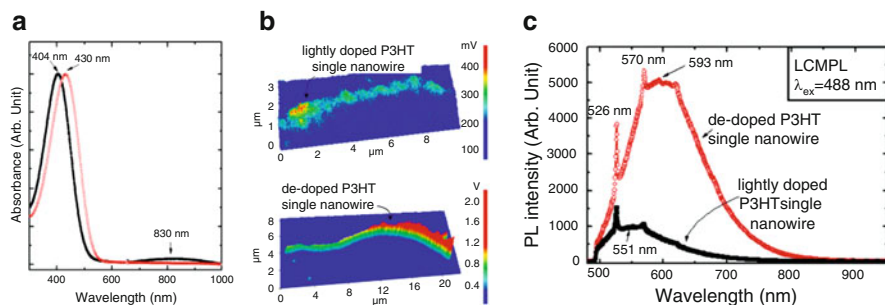


Fig. 11 (a) Normalized UV–vis absorption spectra of P3HT NWs. (b) 3D LCM PL images of isolated single NWs. Color scale bar represents the LCM PL intensities in the unit of measured voltages. (c) Comparison of LCM PL spectra of P3HT NWs. (Reprinted with permission from [42]. Copyright 2007 American Institute of Physics.)

3.1.4 P3HT Nanowires

The dedoping effects of NaOH treatment on electrochemically synthesized P3HT NWs were also reported by Lee and coworkers [42]. Figure 11a shows the normalized UV–vis absorption spectra of P3HT NWs. Shifting of the π – π^* transition peaks and variation of the doping-induced bipolaron peaks were also observed after treatment with HF and NaOH solutions, respectively. The broad bipolaron peak at 830 nm for the HF-treated P3HT NWs was decreased by NaOH treatment as a result of the dedoping effect [41].

Figure 11b shows the 3D LCM PL images of single lightly doped and de-doped P3HT NWs obtained after HF and NaOH treatments, respectively. The LCM PL intensities for these strand were 0.3–0.4 and 1.2–2.3 V, respectively. The LCM PL intensity of the de-doped P3HT single NW was three to eight times higher than that of the lightly doped NWs. Figure 11c compares the averaged LCM PL spectra of individual lightly doped and de-doped P3HT NWs. The main PL peaks for the isolated lightly doped and de-doped P3HT NWs were observed at 551 nm (green light emission) and 593 nm (yellow–green light emission), respectively. The sharp peaks in the PL spectra at 526 and 570 nm originated from the Raman modes. The integrated area of the LCM PL spectrum of the de-doped P3HT NW was approximately six times larger than that of the lightly doped P3HT NW.

Light-emitting polymer NTs and NWs synthesized through electrochemical polymerization exhibit doped states owing to dopant-assisted polymerization [39]. Analysis of the UV–vis spectra showed that the doping level of NTs and NWs can be controlled by varying the synthetic temperatures as well as the applied current or voltage, which directly influence the intrinsic optical properties of the nanostructures. In addition, the solvent used for removing the Al_2O_3 template is also an important determiner of the doping characteristics of the NTs and NWs.

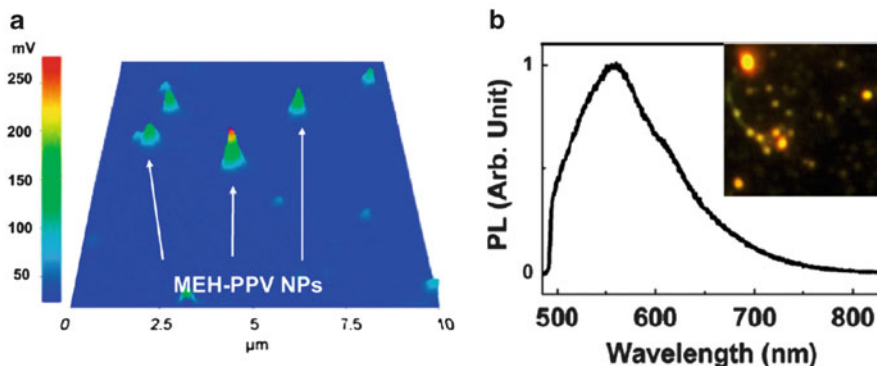


Fig. 12 (a) 3D LCM PL image of isolated MEH-PPV NPs. Color scale bar represents the LCM PL intensities in the unit of measured voltages. (b) LCM PL spectrum of MEH-PPV single NP. *Inset*: color CCD image of the NPs. (Reproduced with permission from [51]. Copyright 2009 American Chemical Society.)

3.2 Nanoparticles Prepared by Reprecipitation

3.2.1 MEH-PPV Nanoparticles

The nanoscale and solid-state optical properties of MEH-PPV NPs fabricated by reprecipitation have been reported [51]. Figure 12a shows a 3D LCM PL image of a single MEH-PPV NP. The LCM PL intensity of a single MEH-PPV NP was measured at ~ 267 (± 17.7) mV, which is the average over 100 different NPs. Figure 12b shows the LCM PL spectrum of the MEH-PPV NP. The main PL peak was observed at ~ 560 nm, which corresponds to the π - π^* transition peak of MEH-PPV observed at ~ 490 nm [51, 73, 74]. These results are reflected in the yellow–orange light emission seen in the color CCD image in the inset of Fig. 12b. In addition, the LCM PL peak of MEH-PPV NPs in the solid state (~ 578 nm) was blue-shifted compared with the solution PL peak [51]. This is attributed to the reduction in the conjugation length due to the steric confinement of NPs, which results in bending or kinking of the polymer backbone [73, 74], as well as to oxidation of NPs in air [75].

3.3 Electrospun Nanowires

3.3.1 Nanowires of MEH-PPV Derivatives

Di Benedetto et al. reported the optical properties of electrospun NWs of MEH-PPV and various derivatives such as poly{[2-methoxy-5-(2-ethylhexyloxy)-1,4-(1-cyanovinyl)phenylene]-*co*-[2,5-bis(*N,N'*-diphenylamino)-1,4-phenylene]},

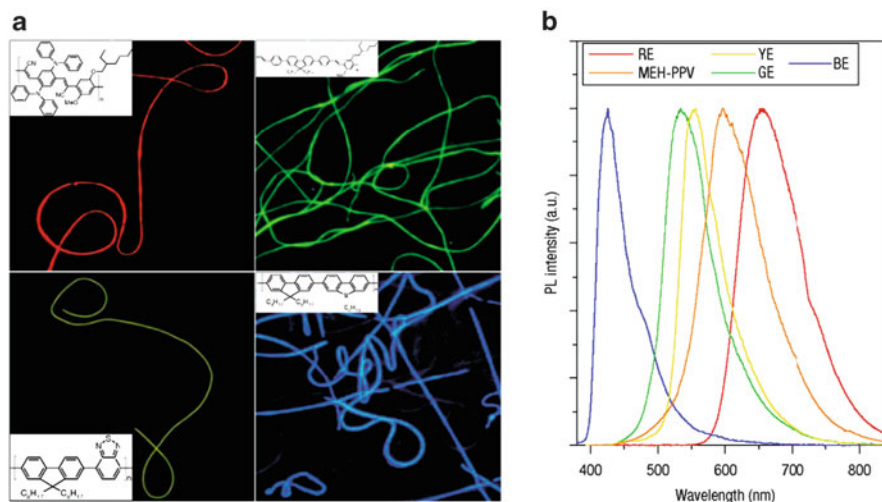


Fig. 13 (a) Fluorescence microscope images of electrospun light-emitting polymer NWs. *Insets:* chemical structure of each light-emitting polymer. (b) Normalized PL spectra of the corresponding samples. (Reproduced with permission from [76]. Copyright 2008 Nature Publishing Group.)

poly{[9,9-dioctylfluorenylene-2,7-diyl]-*co*-[1,4-diphenylenevinylene-2-methoxy-5-(2-ethylhexyloxy)-benzene]}, poly{[9,9-dioctylfluorenyl-2,7-diyl]-*co*-[1,4-benzo-(2,1',3)-thiadiazole]}, and poly[(9,9-dioctylfluorenyl-2,7-diyl)-*alt-co*-(9-hexyl-3,6-carbazole)] [76]. These MEH-PPV derivatives are denoted as RE, GE, YE, and BE, respectively, according to the color of the light they emit. Figure 13a shows the fluorescence microscope images of the electrospun NWs of MEH-PPV derivatives. The images show well-defined colors that agree with the corresponding PL spectra shown in Fig. 13b. These results indicate that the optical properties of various light-emitting polymer NWs can be successfully controlled by the molecular design.

4 Post-synthetic Treatments for Modification of Nanostructure Characteristics

In this section, we introduce post-synthetic treatments that enable further modification of the physical properties such as the structural, electrical, and optical properties of the as-prepared light-emitting polymer nanostructures. Of the various methods of controlling the intrinsic characteristics of nanostructures, we discuss the electrochemical doping and dedoping process using cyclic voltammetry (CV) and unfocused electron (E)-beam irradiation. Hydrothermal treatment of undoped NPs is presented, which involves application of external pressure and heat to NPs. Finally, we describe hybridization with nanoscale

metals, which allows drastic variations in the optical properties by exploiting the surface plasmon resonance (SPR) coupling effect between the light-emitting polymer and the nanoscale metal.

4.1 Electrochemical Doping and Dedoping: Cyclic Voltammetry

Electrochemical reduction and oxidation (redox) using CV is widely used to control the doping characteristics of π -conjugated polymers and their nanostructures [77–80]. Doping of π -conjugated polymers induces changes in structure and electronic state owing to intercalation of dopants between the polymeric chains. These structural modifications induce variations in the π -conjugation length, polymeric chain alignment, and intra-/interchain interactions, which in turn directly influence the light absorption and emission properties.

Park et al. reported that additional doping and dedoping of the as-prepared P3MT NTs and PEDOT NWs can be accomplished through electrochemical means by controlling the applied potentials and scan rates using CV in a mixture of an ionic liquid and a CH_3CN solution without monomers [43, 65]. It is noted that 1-butyl-3-methylimidazolium hexafluorophosphate (BMIMPF_6) is an environmentally stable and recyclable ionic liquid that has shown negligible loss of electroactivity when used as a dopant [77].

4.1.1 P3MT Nanotubes

Figure 14a shows the normalized UV–vis absorption spectra of P3MT NTs at different doping levels. The π – π^* transition peaks were observed at ~ 385 nm for all the P3MT NTs. Broad bipolaron peaks due to doping were observed near 750–800 nm [81]. The relative intensity ratio of the bipolaron peak to the π – π^* transition peak for the doped-P3MT NTs was estimated to be 0.67, 0.52, 0.25, and 0.04, depending on the degree of additional doping or dedoping. The relative integrated area ratio of the bipolaron peak to the π – π^* transition peak was 0.67, 0.54, 0.22, and 0.01, respectively. On the basis of the UV–vis absorption spectra, the various doped-P3MT NTs are denoted as doped-P3MT(0.04), doped-P3MT(0.25), doped-P3MT(0.52), and doped-P3MT(0.67) NTs, where the number in brackets represents the relative doping level. The relatively small ratios of intensity or area of the bipolaron peaks compared with those of the π – π^* transition peaks imply that the P3MT NTs were lightly doped systems.

Figure 14b shows a comparison of the LCM PL spectra of a single P3MT NT with various doping levels: doped-P3MT(0.04), doped-P3MT(0.25), doped-P3MT(0.52), and doped-P3MT(0.67). The peak intensity and area of the LCM PL spectra of these single strands gradually increased up to 14 times as the doping level decreased. Two characteristic peaks in the LCM PL spectra for the P3MT materials were observed at 640 and 685 nm.

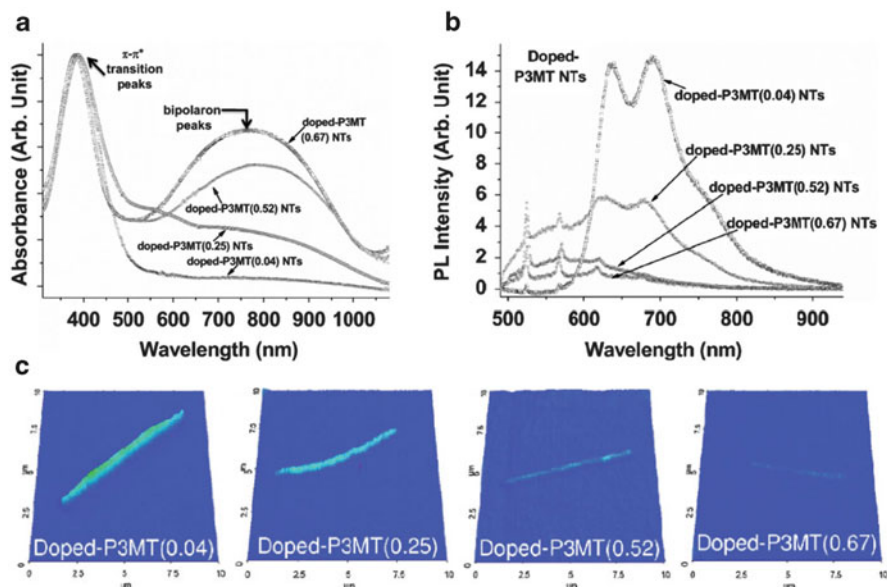


Fig. 14 (a) Comparison of UV-vis absorption spectra of P3MT NTs with different doping levels. (b) LCM PL spectra and (c) 3D LCM PL images of the corresponding samples. (Reproduced with permission from [65]. Copyright 2008 Wiley-VCH.)

Figure 14c shows the LCM PL images for isolated single doped-P3MT NTs with different doping levels under the same LCM experimental conditions. The color scale bar with the unit of voltage at the left-hand side of Fig. 14c represents the measured LCM PL intensity. The measured voltages of the LCM PL intensity for doped-P3MT(0.04), doped-P3MT(0.25), doped-P3MT(0.52), and doped-P3MT(0.67) single NTs were about 40–44, 26–31, 12–16, and 5–8 mV, respectively. These results indicate that the LCM PL intensity of the P3MT NTs decreased with an increase in the doping levels, which is attributed to PL quenching by the dopant or the counter-ions.

4.1.2 PEDOT Nanowires

PEDOT, one of the most popular π -conjugated polymers, has been intensively studied for developing nanoscale materials as well as for application to various nanodevices such as biosensors and electrochromic devices, and for drug delivery [82–84]. However, studies on PEDOT nanomaterials and bulk films have mainly focused on their electrical and structural properties and on the various applications of the conducting form of the material (i.e., doped PEDOT systems). The light-emitting characteristics of doped and de-doped PEDOT nanomaterials were first reported by Park et al. in 2008 [43].

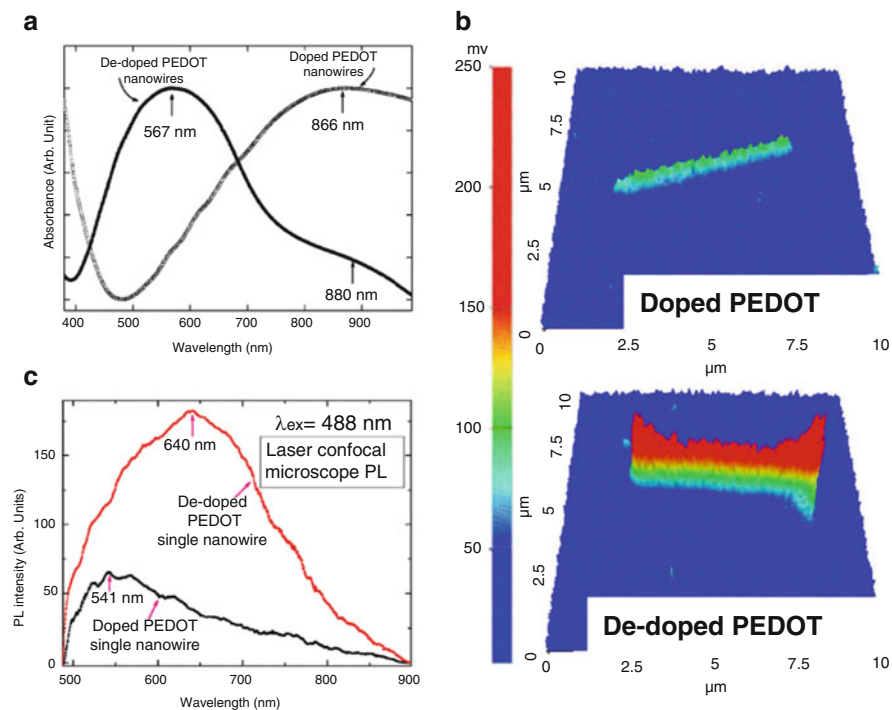


Fig. 15 (a) Comparison of UV–vis absorption spectra of doped and de-doped PEDOT NWs. (b) 3D LCM PL images and (c) LCM PL spectra of isolated single NWs. Color scale bar represents the LCM PL intensities in the unit of measured voltages. (Reprinted with permission from [43]. Copyright 2008 Elsevier B.V.)

Figure 15a shows the normalized UV–vis absorption spectra of electrochemically doped and de-doped PEDOT NWs. A broad electrochemical reduction peak was observed at ~ 1.0 V. The first cycle of the cyclic voltammogram exhibited a well-defined reduction peak, showing that a stable reduction process occurs in a solution of the ionic liquid BMIMPF₆ [77]. For de-doped PEDOT NWs, the π – π^* transition peak was observed at ~ 567 nm, and a weak bipolaron peak was observed at ~ 880 nm, as shown in Fig. 15a. For doped PEDOT NWs, a broad bipolaron band was observed at ~ 866 nm, and the π – π^* transition peak disappeared owing to the doping effect, as shown in Fig. 15a. The π – π^* transition of a pristine PEDOT sample is usually observed at ~ 610 nm and, for doped PEDOT systems, a long-wavelength absorption appears above 900 nm owing to the narrow band gap [85]. Compared with bulk PEDOT [85], the PEDOT NWs that were de-doped and doped by CV exhibited relatively blue-shifted π – π^* transition and bipolaron peaks.

As shown in Fig. 15b, the LCM PL spectra of single doped and de-doped PEDOT NWs were compared under the same experimental conditions. The maximum LCM PL peaks for the single doped and de-doped PEDOT NWs were observed at ~ 541 nm (green light emission) and ~ 640 nm (orange–red light emission), respectively.

The LCM PL peak of the PEDOT single NW was blue-shifted after doping. The PL peaks of pristine PTh and P3HT film samples are usually observed at 610 and 640 nm (i.e., orange–red light emission), respectively [84]. The LCM PL peak intensity of the single de-doped PEDOT NW increased up to a maximum of approximately threefold as compared with that of the doped PEDOT NW, as shown in Fig. 15b.

Figure 15c shows 3D LCM PL images of isolated single doped and de-doped PEDOT NWs. The PL image of the single de-doped PEDOT NW is brighter than that of the doped PEDOT NW. The measured voltages of the PL intensity for the doped and de-doped PEDOT single NWs were 60–90 and 180–260 mV, respectively. The PL intensity of the de-doped PEDOT single NW was two to three times higher than that of the doped PEDOT NW because of the reduction in PL quenching through the dedoping process.

4.2 Unfocused E-Beam Treatment

Hong et al. reported the dedoping and conformational effects of unfocused E-beam treatment of NTs and NWs of light-emitting and conducting polymers [67, 86, 87]. Compared with the conventional solution-based techniques for the control of doping level, such as chemical doping [31–33] or electrochemical redox by CV [79, 80], E-beam treatment enables control of the optical properties of light-emitting polymer nanostructures in a quantitative manner through adjustment of the E-beam parameters such as dosage and/or energy. This approach has the advantages of a relatively simple procedure and reduced contamination by solvents.

An unfocused E-beam from a linear electron accelerator was directed onto P3MT NTs along the length direction. The energy of the E-beam was fixed at 1 MeV, and the dosage of the E-beam was varied in the range from 1.6×10^{13} to 8.0×10^{16} electrons/cm². The treatment was performed in air at atmospheric pressure and room temperature. The heating effect produced by the E-beam was compensated for by air cooling [67]. Figure 16a shows the normalized UV–vis absorption spectra of P3MT NTs in the pristine state (i.e., before E-beam treatment) and after treatment with an unfocused E-beam of different dosages. For the pristine P3MT NTs, a broad and relatively strong bipolaron peak and relatively weak π – π^* transition peak were observed at ~ 800 and 400 nm, respectively, which indicate highly doped states. As the dose of the E-beam irradiation was increased from 1.6×10^{13} to 8.0×10^{16} electrons/cm², the doping-induced bipolaron peak considerably decreased and the π – π^* transition peak was shifted from 400 to ~ 550 nm. It is known that there exist two helical configurations for the polymeric chain in P3MT, namely, the coil-like and rod-like configurations, which correspond to the peaks at 400 and ~ 550 nm in the UV–vis absorption spectra, respectively [88–90]. From Fig. 16a, it is seen that rod-like configurations with π – π^* transition peaks at ~ 550 nm were observed after E-beam treatment with a dose of 4.8×10^{16} to 8.0×10^{16} electrons/cm². The π – π^* transition peaks of the electrochemically de-doped P3MT NTs were not very far from their original positions [65].

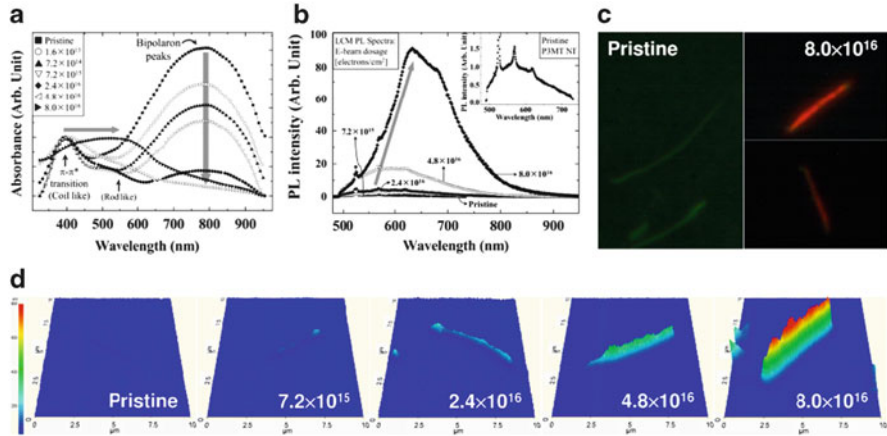


Fig. 16 Comparison of (a) UV-vis absorption spectra, (b) LCM PL spectra, and (c) color CCD images of single P3MT NTs in pristine state and after treatment with a 1-MeV E-beam. (d) 3D LCM PL images of P3MT NTs treated with an unfocused E-beam dose of 7.2×10^{15} to 8.0×10^{16} electrons/cm². Color scale bar represents the LCM PL intensities in the unit of measured voltages. (Reproduced with permission from [67]. Copyright 2009 Wiley-VCH.)

Figure 16b shows the LCM PL spectra for an isolated single P3MT NT in the pristine state and after treatment with an unfocused E-beam of different dosages. With increasing dosage of the E-beam, the intensity of the LCM PL spectra rapidly increased up to about 90 times that of the pristine P3MT NTs. Its peak was gradually red-shifted from about 550 nm for the pristine P3MT NT to about 620 nm after treatment with a 1-MeV E-beam dose of 8.0×10^{16} electrons/cm², as shown in Fig. 16b.

Figure 16c shows color CCD images of the NTs in the pristine state and after treatment with a 1-MeV E-beam dose of 8.0×10^{16} electrons/cm². The pristine P3MT NTs emitted green light with a relatively low brightness. After irradiation with the E-beam, the luminescence color was dramatically changed from green to red. Moreover, the luminescent intensity clearly increased.

Figure 16d shows the 3D LCM PL images under identical LCM experimental conditions for an isolated single P3MT NT in the pristine state and after E-beam irradiation with different E-beam dosages. As the dose of the 1-MeV E-beam was increased from 7.2×10^{15} to 8.0×10^{16} electrons/cm², the LCM PL intensity of the isolated single P3MT NTs dramatically increased. The averaged voltage of the LCM PL intensity in the pristine state was $10 (\pm 2.8)$, and after irradiation with a 1-MeV E-beam it was $22 (\pm 2.1)$, $34 (\pm 2.5)$, $127 (\pm 3.8)$, and $716 (\pm 4.6)$ mV, corresponding to doses of 7.2×10^{15} , 2.4×10^{16} , 4.8×10^{16} , and 8.0×10^{16} , respectively. These results indicate that E-beam treatment causes an increase in PL efficiency and alters the luminescence color of P3MT NTs. The significant enhancement in PL intensity might originate from the dedoping effect.

4.3 Hydrothermal Treatment

Hydrothermal processes have been used to synthesize metal oxides such as titanium oxide and zinc oxide and to modify the material properties [26, 91]. Zhou et al. reported that hydrothermal treatment converted graphene oxide to a stable graphene solution [92]. Jung et al. studied the structural transformation of organic copper phthalocyanine NWs into hollow rectangular NTs during a hydrothermal process [93]. Recently, Lee et al. reported that the structural and optical properties of P3HT NPs prepared by reprecipitation [48] can be controlled through hydrothermal treatment at different temperatures [94]. In their study, an autoclave served as the chamber for the hydrothermal process. Pristine (i.e., before hydrothermal treatment) P3HT NPs dispersed in deionized water were placed in a Teflon beaker in the chamber, which was heated in an oven to a temperature between 60°C and 150°C. In this process, external pressure is applied on the P3HT NPs, roughly estimated to be 15 bar at 100°C [95]. Then, the chamber was allowed to cool naturally. A homogenous dispersion of NPs was obtained by sonicating the P3HT NP solution with a high-power ultrasonicator.

Figure 17a and its insets show the SEM and TEM images, respectively, of P3HT NPs in the pristine state and after hydrothermal treatment at various temperatures. The numerical labels of the hydrothermally treated (HT) samples (HT060, HT090, HT110, HT120, HT130, and HT150) indicate the temperature of treatment in degrees Celsius. The diameters of the pristine, HT060, HT110, and HT150 P3HT NPs were 77 (± 11), 88 (± 11), 184 (± 50), and 471 (± 107) nm, respectively. The shape and degree of aggregation for P3HT NPs treated at temperatures of 110°C and above were clearly different from those of the pristine and HT060 NPs.

Figure 17b shows the normalized UV-vis absorption spectra of the pristine and hydrothermally treated P3HT NPs. The absorption peaks were observed at 510, 550, and 610 nm for the pristine P3HT NPs, which coincide with those of spin-coated P3HT films [90, 96, 97]. The UV-vis absorption spectra changed with increasing hydrothermal temperature, as shown in Fig. 17b: the peaks shifted to longer wavelengths and their relative intensities changed. The absorption peak at ~510 nm was dominant for the pristine, HT060, and HT090 samples. However, with increasing temperature, the absorption intensity at ~550 nm gradually increased, as seen for the HT110, HT120, and HT130 samples. The peak at 610 nm, corresponding to the 0-0 transition, was the strongest for the HT150 P3HT NPs. A long-wavelength tail also progressively developed with increasing hydrothermal temperature owing to the scattering effect. These results are attributed to the interchain interactions and ring planarity in the P3HT main chains that are strengthened owing to the higher pressure applied during the hydrothermal process with increasing temperature [98-100].

Figure 17c shows the normalized LCM PL spectra for single pristine and HT P3HT NPs averaged over 20 different dry NPs. The intensity and position of the 0-1 emission peak at 692-708 nm were different for the individual NPs and varied with the hydrothermal temperature. Its dominance increased for the HT060 and HT110

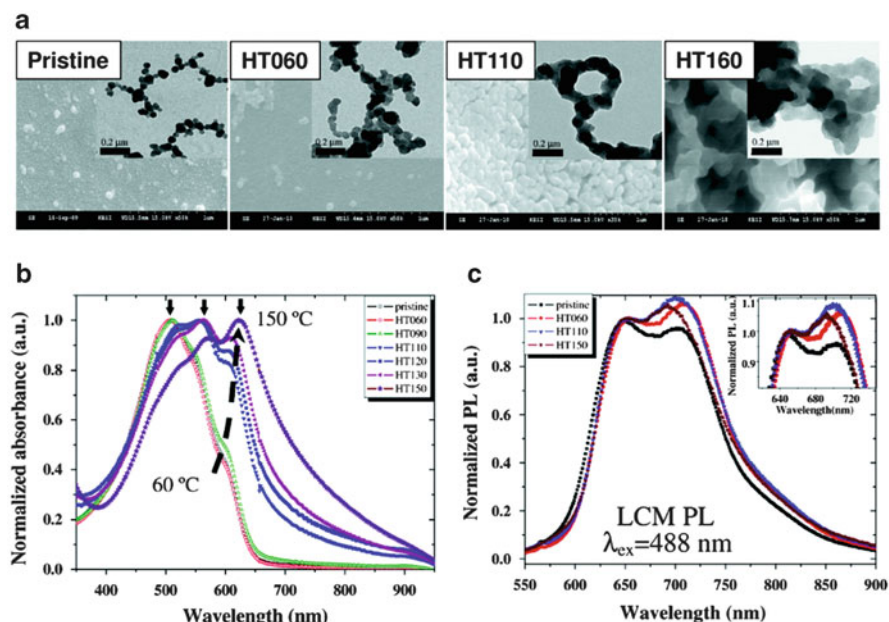


Fig. 17 (a) SEM images of P3HT NPs in pristine state and after hydrothermal treatment at various temperatures. *Inset*: TEM images of corresponding NPs. Comparison of (b) UV-vis absorption and (c) LCM PL spectra of P3HT NPs in pristine state and after hydrothermal treatment at various temperatures. (Reproduced with permission from [94]. Copyright 2011 Institute of Physics.)

samples, in qualitative agreement with the changes in the UV-vis absorption spectra. The 0-1 to 0-0 PL intensity ratio was maximum for the HT110 sample. The external pressure in the hydrothermal process strengthened the interchain interactions, leading to the increase in the degree of tilt of the alkyl side chains and the planarity of the thiophene rings, and a decrease in the distance of interchain π -stacking. The LCM PL spectra suggest that the interchain interactions strengthened (i.e., the interchain distance decreased) as the hydrothermal temperature was increased from 60 to 110 °C; however, severe conformational changes might have occurred in the P3HT chains during hydrothermal processing at temperatures of 130 °C and above, leading to the decrease in the 0-1 emission for the HT150 sample.

4.4 Hybridization with Metal Nanostructures

Hybridization between π -conjugated polymers and metals at the nanoscale level has been used for luminescence enhancement and to realize biosensing through SPR coupling [6, 64, 65, 101, 102]. The surface plasmon defines a coherent excitation of free electrons in metal nanostructures interacting with an incident electromagnetic

wave, resulting in collective in-plane oscillations [101]. When the dimensions of metal nanostructures, such as the thickness of an NT and diameter of an NP are scaled down to levels comparable to the skin depth, the incident electromagnetic energy is effectively absorbed by light-emitting polymers. Furthermore, SPR coupling in hybrid nanostructures occurs if the surface plasmon absorption energy of the metal matches the photon energy of the light-emitting polymer, which leads to drastic variations in the optical properties of the hybrid nanostructures [6, 64, 65].

4.4.1 Hybrid Double-Layered Nanowires and Nanotubes

The variation in luminescence efficiency and color of hybrid double-layered (HDL) NWs or NTs that were fabricated by coating the surface of light-emitting polymer NWs or NTs with a nanoscale film of metal was reported [103, 104]. Figure 18a–c shows the SEM and TEM images of pristine and HDL-NWs of P3BT/Ni and P3BT/Cu [103]. The formation of two clear layers was observed: the inside and outside layers of the HDL-NWs were P3BT and the metal (Ni or Cu), respectively. The TEM image of an isolated single HDL-NW shows that the total diameter of the hybrid P3BT/Cu NW and the thickness of the external Cu NT were ~ 200 and ~ 10 nm, respectively, as shown in Fig. 18b. The high-resolution (HR) TEM image shows the fine and periodic stripe patterns of the outer metal NT, which match the crystalline structure of Cu (lattice spacing $\cong 0.21$ nm). As shown in the inset of Fig. 18c, the crystalline spots in the selected area electron diffraction (SAED) pattern of the P3BT/Cu HDL-NWs support the conclusion that the outer Cu NT has a crystalline structure in accordance with the HR-TEM results.

Figure 18d, e shows luminescent color CCD and 3D LCM PL images of an isolated single P3BT NW and HDL-NWs of P3BT/Ni and P3BT/Cu. Weak green light emission was observed for the P3BT single NW owing to the lightly doped states, whereas both HDL-NWs (P3BT/Ni and P3BT/Cu) showed bright orange–red light emission, as shown in Fig. 18d. The intensity in the 3D LCM PL image of the P3BT single NW was measured at 22–28 mV. For single HDL-NWs made of P3BT/Ni or P3BT/Cu, the measured voltages of the LCM PL intensities were 1.8–2.3 and 1.5–2.0 V, respectively. The application of the nanoscale Ni or Cu metal coating on the outside of the P3BT NWs led to a 60- to 110-fold increase in the measured voltages of the 3D LCM PL intensities compared with that of the P3BT single NW. Similar results for the HDL-NTs of PTh/metals were reported earlier [64]. Figure 18f shows the averaged LCM PL spectra of corresponding samples. The main LCM PL peak for a single P3BT NW was observed at ~ 544 nm, corresponding to green light emission. With the nanoscale metal coating, the main LCM PL peaks of the HDL-NWs of P3BT/Ni and P3BT/Cu were red-shifted to ~ 635 and ~ 639 nm, respectively, in the range of orange–red light emission. The peak intensity and integrated area of LCM PL spectra significantly increased up to about 80–90 times after hybridization with nanoscale metals [61, 68].

The PL enhancement and color variation of the HDL-NWs are attributed to the energy and charge-transfer effects in SPR coupling. The inset on the right in Fig. 18f

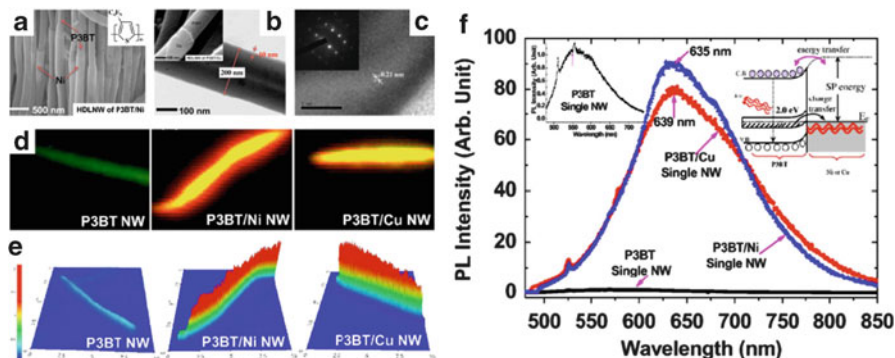


Fig. 18 (a) SEM image of HDL-NWs of P3BT/Ni. *Inset*: chemical structure of a P3BT monomer unit. (b) TEM image of a single P3BT/Cu HDL-NW. *Inset*: magnified SEM image of the same sample. (c) Magnification of HR-TEM image of outside Cu part of a single P3BT/Cu HDL-NW. *Inset*: SAED pattern of the P3BT/Cu HDL-NW. (d) Luminescence color CCD images of P3BT NW (*left*) and HDL-NWs of P3BT/Ni (*middle*) and P3BT/Cu (*right*). (e) 3D LCM PL images of the corresponding samples. (f) LCM PL spectra of an isolated single P3BT NW in the pristine state and HDL-NWs of P3BT/Ni and P3BT/Cu. *Left inset*: magnification of the LCM PL spectrum of a P3BT NW for reference. *Right inset*: energy band diagram explaining the enhancement of PL efficiency and red-shift of the LCM PL peak of the HDL-NWs of P3BT/Ni and P3BT/Cu. (Reproduced with permission from [103]. Copyright 2009 Electrochemical Society.)

illustrates the schematic energy band diagram for HDL-NWs of P3BT/Ni or P3BT/Cu. Because the surface plasmon energies of the nanoscale Ni or Cu were approximately matched by the energy band gap of P3BT (~ 2.0 eV), energy transfer occurs between P3BT and the metals owing to SPR coupling, which leads to enhancement of the PL efficiency of the HDL-NWs. For the electrochemically synthesized P3BT NWs with relatively doped states, the Fermi energy (E_F) of the metal and doping-induced bipolaron states of the P3BT NWs matched with each other. Then, charges could be transferred from the bipolaron band of the lightly doped P3BT NWs to the E_F of the metals. This might explain the dedoping effect and the red-shifted LCM PL peaks for the HDL-NWs of P3BT/Ni and P3BT/Cu. In addition to energy transfer, charge transfer also contributed to the increased PL efficiency [6, 64, 65].

Figure 19a shows a magnified SEM image of an isolated single partial HDL-NT of P3MT/Ni in which only the lower half was coated with Ni by controlling the electrochemical deposition time [104]. The diameters of the P3MT NT section and P3MT/Ni HDL-NT section were ~ 180 and ~ 200 nm, respectively. Figure 19b shows a 3D LCM PL image of an isolated single partial HDL-NT of P3MT/Ni. The averaged PL intensities of the pristine P3MT NT and P3MT/Ni HDL-NT sections were 12–15 and ~ 600 mV, respectively. Figure 19c compares the normalized LCM PL spectrum of the P3MT/Ni HDL-NT section with that of the pristine P3MT NT section. A broad LCM PL peak was observed in the P3MT/Ni HDL-NT section at 625–675 nm. It was ~ 40 times higher than that of the pristine P3MT NT section, excluding the Raman modes detected at 525 and 570 nm.

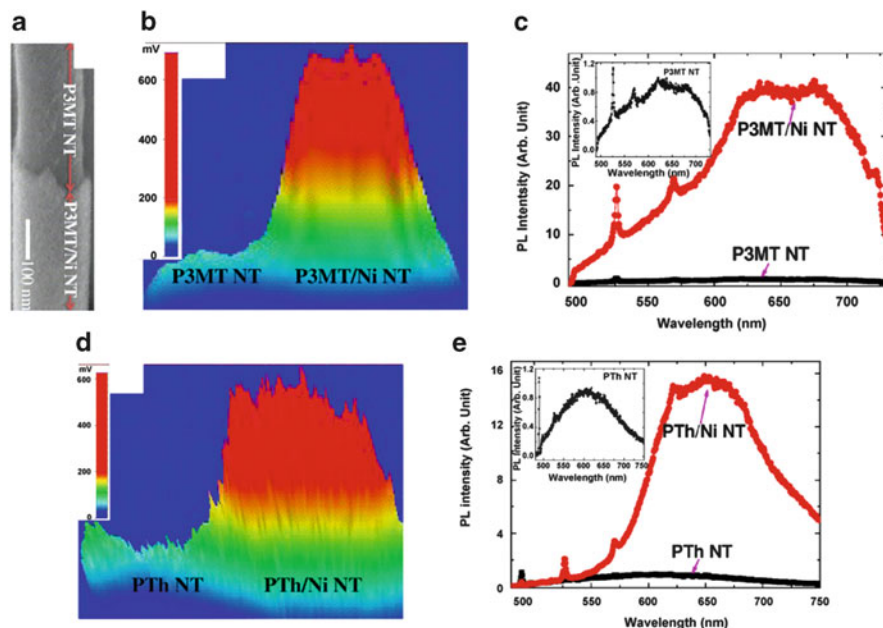


Fig. 19 (a) Magnified SEM image of single partial P3MT/Ni HDL-NT. (b) 3D LCM PL image of partial P3MT/Ni HDL-NT. (c) Comparison of the LCM PL spectra of the pristine and P3MT/Ni HDL-NT sections. *Insets:* magnification of the LCM PL spectrum of the corresponding pristine NTs for reference. (d, e) Corresponding LCM PL data of PTh/Ni. (Reproduced with permission from [104]. Copyright 2009 Elsevier B.V.)

Enhancement of PL efficiency and variation in light-emitting color attributed to hybridization with metal NTs were also observed by using PTh NTs, as shown in Fig. 19d, e. For the pristine PTh NT section, the measured voltages of the LCM PL intensity and the position of the maximum PL peak were 35–40 mV and ~620 nm, respectively. These values were 540–585 mV and ~650 nm for the PTh/Ni HDL-NT section.

4.4.2 Hybridization with Metal Nanoparticles

Recently, hybrid nanostructures using metal NPs have been intensively studied for improving the physical properties and the efficiencies of optoelectronic devices and biosensors [102, 105–113]. Among the various metals, gold (Au) and silver (Ag) have drawn particular attention owing to their strong SPR effect in the visible spectrum [101, 102, 105]. Kim and coworkers reported PL enhancement in hybrid NPs composed of MEH-PPV NP and Au NPs, which was attributed to the SPR-mediated energy transfer effect [51]. Park and coworkers fabricated a hybrid nanostructure comprising functionalized Au NPs attached to the outer surface of electrochemically synthesized P3MT single NT (denoted as P3MT-NT/Au-NPs) [114].

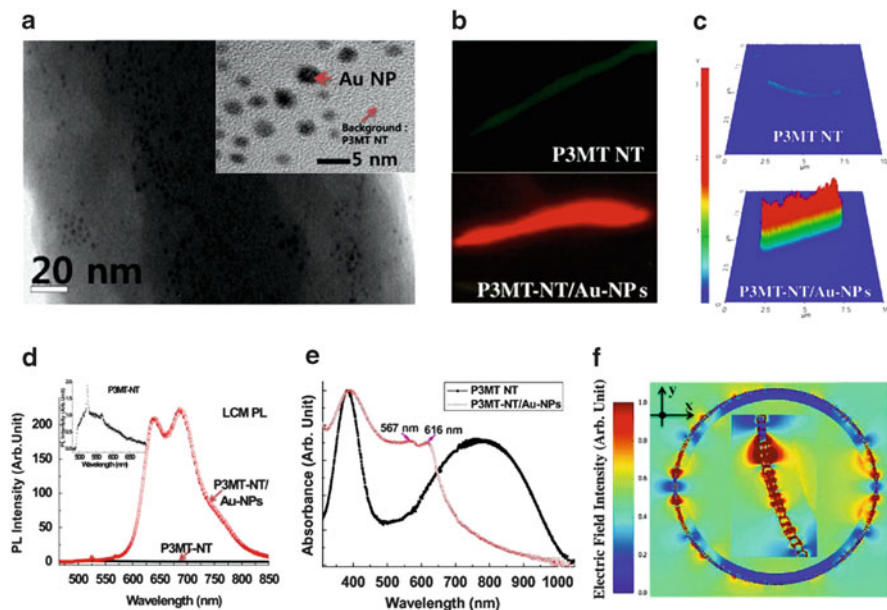


Fig. 20 (a) HR-TEM image of single unit of hybrid P3MT-NT/Au-NPs. *Inset*: magnified HR-TEM image of the corresponding sample. The *small black spots* represent the Au NPs. (b) Color CCD images of a single P3MT NT (*top*) and the hybrid P3MT-NT/Au-NPs (*bottom*). (c) 3D LCM PL image of corresponding samples of (b). (d) Comparison of the LCM PL spectra of a single strand of the P3MT NT and the hybrid P3MT-NT/Au-NPs. *Inset*: LCM PL spectra of single P3MT NT for reference. (e) Normalized UV-vis absorption spectra of the P3MT NT and the hybrid P3MT-NT/Au-NPs. (f) Local electric field distribution of 2D nanostructure model of light-emitting polymer with Au NPs attached, based on the FDTD calculation. *Inset*: magnification of local electric field distribution of the 2D nanostructure of polymer/Au-NPs based on the FDTD calculation. (Reproduced with permission from [114]. Copyright 2010 Elsevier B.V.)

Figure 20a shows a magnified HR-TEM image of a single unit of hybrid P3MT-NT/Au-NPs. Small black spots representing the Au NPs were clearly observed on the surface of the P3MT NT, which was evidence for the formation of hybrid nanostructures of P3MT NT with Au NPs. As shown in the inset of Fig. 20a, the fine and periodic stripe patterns of the Au NPs with diameters of 2–3 nm indicate a crystalline structure of the Au material. In addition, nanoscale gaps of 3–20 nm were observed between the Au NPs.

Figure 20b–d shows the results of luminescence color CCD and LCM PL experiments on a single pristine P3MT NT and the hybrid P3MT-NT/Au-NPs. For the pristine P3MT NT, the averaged intensity of the 3D LCM PL image and the peak position of the LCM PL spectrum were 8–10 mV and ~544 nm, respectively. For the hybrid P3MT-NT/Au-NPs, the PL intensity measured at 2.1–2.5 V had increased up to 210–310 times. The PL spectrum was red-shifted, with two characteristic peaks at 640 and 685 nm. These results are consistent with bright red light emission in the

color CCD image. Comparison of the LCM PL spectra showed a PL enhancement estimated at 220-fold, which shows good agreement with the results in the LCM PL images.

Figure 20e shows the normalized UV–vis absorption spectra of the P3MT NTs and hybrid P3MT-NT/Au-NPs. Typical absorption characteristics were observed for the pristine P3MT NTs with doped states. For the hybrid P3MT-NT/Au-NPs, the intensity of the doping-induced bipolaron peak was considerably decreased, and two new absorption peaks were generated at 567 and 616 nm. These new peaks were assigned to the electrical dipole and quadrupole contributions in the surface plasmons, which resulted from the matching of the Fermi energy (E_F) levels between the P3MT NT and the Au NPs.

Figure 20f shows the electric field distributions in hybrid polymer-NT/Au-NPs according to simulation using the finite-difference time-domain (FDTD) method [51]. By choosing experimental values as the simulation parameters [114], a strong local electric field enhancement in the nanogaps between Au NPs was calculated in the background of the light-emitting P3MT [115–117]. This local electric field enhancement, represented by the red color parts in Fig. 20f and its inset, also contributes to the PL enhancement of the hybrid P3MT-NT/Au-NPs. All the results support the occurrence of energy and/or charge transfer attributed to the SPR coupling effects in the hybrid nanostructures of light-emitting polymers and metals.

5 Applications

In this section, various applications of light-emitting polymer nanostructures are introduced. The application of low-dimensional heterojunction NWs to optoelectronics, photonics, and biotechnologies has received considerable attention [118–124]. Inorganic material-based heterojunction NWs have been reported, and their application to optically reflecting barcode NWs has been investigated [118, 119, 125–130]. This section introduces novel organic-based heterojunction NWs, light-emitting color barcode (LECB)-NWs, and quasi-superlattice NWs made using light-emitting polymers. Solid-state and label-free DNA detection is discussed in terms of PL characteristics. Finally, nano-optoelectronic applications of light-emitting polymer nanostructures, such as rectifying, photo-switching, and photovoltaic effects, are presented.

5.1 Barcodes

Conventional black and white barcodes have been used for the identification of commercial products through optical reflection. For effective identification of nanoscale products with complex physical shapes, the identification sensitivity,

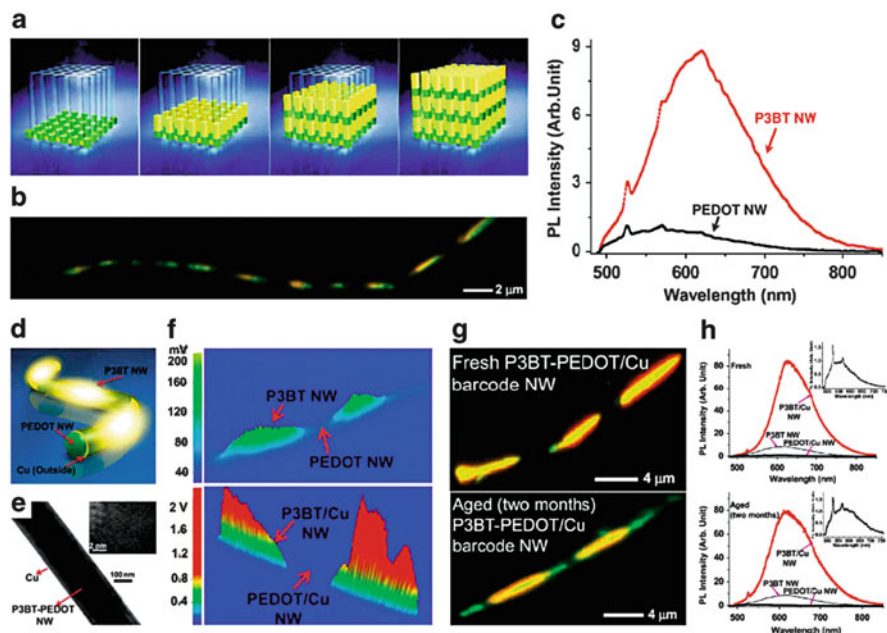


Fig. 21 (a) Sequential electrochemical polymerization method for LECB-NWs. (b) Color CCD image of single P3BT-PEDOT LECB-NW with 22 sections. (c) Comparison of LCM PL spectra of P3BT and PEDOT sections of a single LECB-NW. (d) Nanoscale metal coating on LECB-NW. (e) HR-TEM image of single P3BT-PEDOT/Cu LECB-NW. *Inset*: magnified HR-TEM image of the outside Cu part of a LECB-NW. (f) Comparison of 3D LCM PL images of isolated single LECB-NWs: P3BT-PEDOT (*top*) and P3BT-PEDOT/Cu (*bottom*). (g) Color CCD images of fresh (*top*) and 2-month-aged (*bottom*) P3BT-PEDOT/Cu LECB-NWs. (h) Comparison of LCM PL spectra of P3BT, P3BT/Cu, and PEDOT/Cu sections of the fresh (*top*) and aged (*bottom*) P3BT-PEDOT/Cu LECB-NWs. *Insets*: normalized LCM PL spectra of the fresh and aged PEDOT/Cu sections for reference. (Reproduced with permission from [131]. Copyright 2010 American Chemical Society.)

accuracy, flexibility, and stability of optical barcode nanomaterials must be improved in combination with the development of appropriate detection tools. Park et al. reported on flexible LECB-NWs synthesized by sequential electrochemical polymerization with distinct light-emitting polymers [131].

Figure 21a shows a schematic illustration of LECB-NWs consisting of two different light-emitting polymer NWs. The length and number of repeated units of the polymer NW code sections were controlled by the polymerization conditions in the electrolyte. As an example, a single strand of other P3BT-PEDOT LECB-NWs having a total of 22 sections is shown in the color CCD image in Fig. 21b. To fabricate the 22 sections of the LECB-NWs, 11 dippings were performed per electrolyte and alternating dipping was employed. The lengths of the P3BT and PEDOT NW sections were controlled to be 1–2 μm by electrochemical polymerization for 60–90 s, with an applied current density of 0.6 mA/cm^2 for P3BT and 0.2–0.4 mA/cm^2 for PEDOT.

Figure 21c shows the LCM PL spectra of the P3BT and PEDOT sections of the same single LECB-NW. The LCM PL peaks for the P3BT and PEDOT sections of the same single NW were detected at ~ 626 nm (i.e., orange–yellow light emission) and 554 nm (i.e., green light emission), respectively. The LCM PL peak intensity and integrated area of the sections of the P3BT NW were approximately nine times higher than those of the PEDOT NW.

Enhanced luminescence efficiency can be expected for polymer-based light-emitting NWs with a nanoscale metal coating, because of energy transfer via SPR coupling [64, 103]. Figure 21d shows a schematic illustration of an LECB-NW comprising nanoscale Cu metal-coated P3BT-PEDOT (denoted as P3BT-PEDOT/Cu). The formation of the hybrid P3BT-PEDOT/Cu LECB-NWs was confirmed through HR-TEM experiments, as shown in Fig. 21e. From the magnified HR-TEM image, the total diameter of the single P3BTPEDOT/Cu LECB-NW and thickness of the outside Cu NT were found to be ~ 200 and ~ 10 nm, respectively. The fine and periodic patterns of the outer tube are attributed to the crystalline structure of the Cu material, as shown in the inset of Fig. 21e.

Figure 21f compares the 3D LCM PL images of isolated single P3BT-PEDOT and P3BT-PEDOT/Cu LECB-NWs under the same LCM experimental conditions. The measured voltages of the LCM PL intensities of the hybrid P3BT/Cu and PEDOT/Cu sections were 1.8–2.0 V and 26–30 mV, whereas those of the P3BT and PEDOT sections without the Cu coating were 140–180 and 22–25 mV, respectively. The measured voltages of the LCM PL intensities for the hybrid P3BT/Cu sections were approximately 10–14 times higher than those of the P3BT sections. The surface plasmon energy (~ 2.1 eV or 585 nm) of the nanoscale Cu closely matched the emissive photon energy of the P3BT materials. Thus, SPR coupling occurred, which induced energy transfer between the nanoscale Cu and P3BT materials [103]. This explains the considerable enhancement in the PL efficiency for the hybrid P3BT/Cu sections.

Figure 21g shows color CCD images of single P3BT-PEDOT/Cu LECB-NW in the fresh state and after aging by exposure to the atmosphere for 2 months. Green light emission was observed from the PEDOT/Cu sections of the aged LECB-NWs, whereas orange–yellow light emission was dominant for the P3BT/Cu sections of the fresh LECB-NWs. These results imply that the Cu metal-coated P3BT-PEDOT LECB-NWs are promising optical barcode NWs because of their highly sensitive light emission and long-term stability for identification. These results were confirmed by measurements of the LCM PL spectra, as shown in Fig. 21h. The LCM PL peak positions and intensities of the aged samples were found to be comparable with those of the fresh samples because of the protection from oxidation given by the nanoscale Cu coating.

LECB-NWs consisting of three different light-emitting polymers (P3MT, P3BT, and PEDOT) coated with nanoscale Cu were fabricated. Red, orange–yellow, and green luminescence were observed corresponding to the P3MT/Cu, P3BT/Cu, and PEDOT/Cu sections of the same LECB-NW, respectively, as shown in the top image of Fig. 22a. In the color CCD image for the mixture of two different LECB-NWs, the three luminescence colors (red, orange–yellow, and green) of the

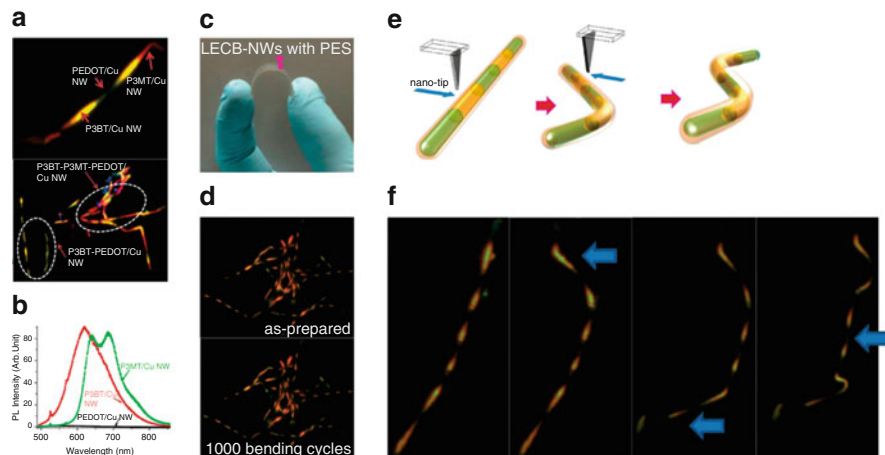


Fig. 22 (a) Color CCD images of P3MT-P3BT-PEDOT/Cu single LECB-NW (*top*) and mixture of P3MT-PEDOT/Cu and P3BT-P3MT-PEDOT/Cu LECBNWs (*bottom*). (b) LCM PL spectra of P3MT/Cu, P3BT/Cu, and PEDOT/Cu sections of single P3BT-P3MT-PEDOT/Cu LECB-NW. (c) Photograph of P3BT-PEDOT/Cu LECB-NWs on bended PES substrate. (d) Color CCD images of P3BT-PEDOT/Cu LECB-NWs on PES substrate as-prepared (*top*) and after 1,000 bending cycles (*bottom*). (e) Flexibility experiments for LECB-NWs through nanotip impetus. (f) Color CCD images of single P3BT-PEDOT/Cu LECB-NW during the applied impetus. The arrows represent the positions of the applied nanotip impetus. (Reproduced with permission from [131]. Copyright 2010 American Chemical Society.)

P3BT-P3MT-PEDOT/Cu LECB-NWs can be selectively distinguished from the two luminescence colors attributed to P3BT-PEDOT/Cu LECB-NWs, as shown in the bottom image of Fig. 22a.

Figure 22b compares the LCM PL spectra of the P3MT/Cu, P3BT/Cu, and PEDOT/Cu sections of the same LECB-NW. The LCM PL peaks for the P3MT/Cu, P3BT/Cu, and PEDOT/Cu sections were detected at 640–685 nm (i.e., red light emission), 620 nm (i.e., orange–yellow light emission), and ~545 nm (i.e., green light emission), respectively. The LCM PL peak intensity and integrated area of the sections of the P3MT/Cu NW and the P3BT/Cu NW were approximately 85 and 90 times higher than that of the PEDOT/Cu NW, respectively.

Figure 22c shows a photograph of the bending of NWs fixed onto a polyethersulfone (PES) flexible substrate. The alternating orange–yellow and green emissions from the P3BT-PEDOT/Cu LECB-NWs on the PES substrate are clearly observed in the color CCD image in Fig. 22d. The flexibility of these NWs was investigated by applying a nanotip impetus to some parts of the NW. Depending on the position of the nanotip impetus (as shown in Fig. 22e), folding and unfolding of the LECB-NW was accomplished, implying that the NW is flexible (as shown in Fig. 22f). These results imply that the P3BT-PEDOT/Cu LECB-NWs can be promising optical barcode NWs that are both durable and flexible.

5.2 Focused E-Beam Treatment: Fine Barcodes and Quasi-superlattice

Focused E-beam irradiation has been used for precisely tailoring the optical and structural properties of organic nanostructures at the nanoscale level [132, 133]. Recently, Hong et al. reported that individual light-emitting P3MT NWs can be tailored successfully to contain multiple 1D serial sections, similar to a quasi-superlattice NW [62]. These sections can have different lengths and characteristics, which can be modified precisely through treatment with a focused E-beam. The spot size of the focused E-beam was adjusted between 50 and 100 nm, and the step size of the focused E-beam irradiation was 2.4 nm, as shown in Fig. 23a.

Figure 23b, c shows the nanoscale optical properties of individual treated P3MT NWs measured by CCD and LCM PL experiments. The PL color of the sections of the pristine P3MT NW remained at the original green with relatively low brightness. When designated positions of the single NW were irradiated with a focused E-beam dose of 7.5×10^{16} electrons/cm², the PL color changed from green to yellow, and the emission intensity was clearly enhanced, as shown in the left image of Fig. 23b. The LCM PL intensities of the treated sections (dose of 7.5×10^{16} electrons/cm²) were approximately 12 times higher than those of the pristine P3MT NW. When the dose was increased to 2.5×10^{17} electrons/cm², the PL color of the treated P3MT NW sections changed to bright red (middle image of Fig. 23b), and a significant increase (~31 times) in the light-emission intensity was confirmed from the LCM PL images. When the focused E-beam dose was increased to 2.5×10^{18} electrons/cm², the PL intensity of the treated sections decreased and bright yellow–green emission was observed from the pristine sections of the same NW (right images of Fig. 23b, c). The results indicate the existence of a critical E-beam dose (ED_C) for modification of the optical properties of P3MT NWs and for E-beam energy transfer along the NWs. The size of the sections in a P3MT NW treated with a focused E-beam can be controlled on the basis of the designed patterns (including size and position). In the left and middle images of Fig. 23b, the lengths of the treated sections on the NW were 1 and 2 μm , respectively. The lengths of the treated sections were also adjusted to 0.25, 0.5, 1, 2, 3, 4, 5, and 6 μm in the same NW.

The averaged LCM PL intensities of the NW sections, as obtained from the line profile of the 3D LCM PL images, changed considerably with the E-beam dose, as shown in Fig. 23d. The LCM PL intensity of the pristine P3MT NW was six photon counts and those of the pristine sections in the treated P3MT NW were 7, 34 (± 1), 265 (± 5), and 326 (± 14) photon counts for doses of 7.5×10^{16} , 2.5×10^{17} , 2.5×10^{18} , and 1.0×10^{19} electrons/cm², respectively. The LCM PL intensities of the treated NW sections were 70 (± 3), 185 (± 6), 24 (± 1), and 3 (± 1), respectively, for these doses.

The LCM PL peak was gradually red-shifted from 520–530 nm for the pristine NW to approximately 560 and 590–600 nm for the NW sections treated with doses of 7.5×10^{16} and 2.5×10^{17} electrons/cm², respectively, as shown in Fig. 23e. The intensities of the LCM PL peaks of the treated sections with these doses were

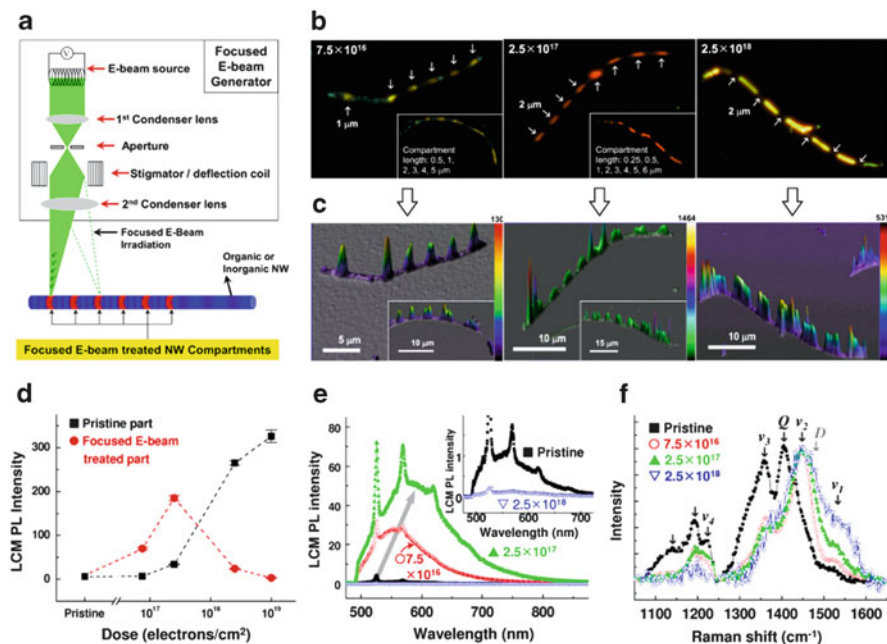


Fig. 23 (a) Focused E-beam treatment at designated positions of a single NW. (b) Color CCD images of single P3MT NWs treated with focused E-beam doses of 7.5×10^{16} electrons/cm² (left), 2.5×10^{17} electrons/cm² (middle), and 2.5×10^{18} electrons/cm² (right). *Insets*: Images of focused E-beam-treated P3MT NWs with different section lengths. The *arrows* indicate the treated sections. (c) 3D LCM PL images of corresponding samples in (b) and their *insets*. The color scale bar on the *right* represents the photon counts. (d) Averaged LCM PL intensity of P3MT NW sections treated with a focused E-beam as a function of dose. (e) LCM PL spectra of the pristine P3MT NW sections and of sections treated with various focused E-beam doses. *Inset*: magnified LCM PL spectra of a section treated with a high dose of 2.5×10^{18} electrons/cm². (f) Normalized micro-Raman spectra for pristine and treated P3MT NW sections at various doses. (Reproduced with permission from [62]. Copyright 2011 Wiley-VCH.)

enhanced up to 25 and 50 times that of the pristine NW, respectively. Below the ED_C , the positions and intensities of the LCM PL peaks were red-shifted and increased with the E-beam dose. However, the emission intensity of the sections treated with a dose higher than the ED_C was considerably lower (inset of Fig. 23e). Therefore, the PL color and intensity of single P3MT NWs can be tailored precisely at the nanoscale level as a function of the focused E-beam dose.

Figure 23f shows the micro-Raman spectra of pristine and treated P3MT NW sections and reveals the structural and doping characteristics. Significant differences in the micro-Raman spectra associated with the focused E-beam treatment were observed in the range of 1,050–1,650 cm⁻¹. The intensities of the Raman peaks at 1,192, 1,223, and 1,361 cm⁻¹, corresponding to C_β-H bending, antisymmetric C_α-C_α ring stretching, and C_β-C_β ring stretching deformation modes, respectively [67, 68, 134], decreased with increasing E-beam dose [67].

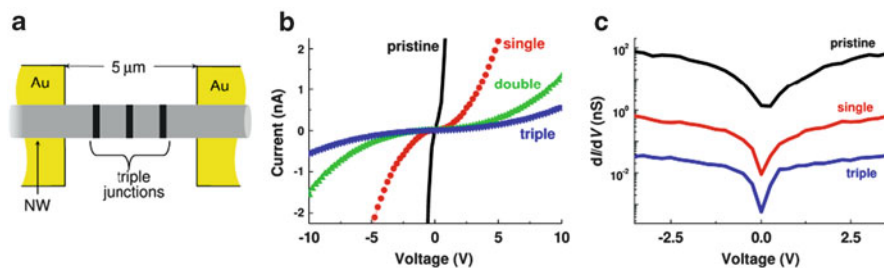


Fig. 24 (a) Diagram of NW with triple junctions on Au electrodes. (b) Comparison of I – V characteristic curves of pristine and treated single P3MT NWs with various numbers of serial junctions. (c) Voltage dependence of differential conductance between pristine and treated single P3MT NWs with various numbers of junctions. (Reproduced with permission from [62]. Copyright 2011 Wiley-VCH.)

The intensity of the doping-induced Q mode at $1,404\text{ cm}^{-1}$ decreased gradually with increasing E-beam dose. The intensities, positions, and line widths of the Raman peaks at $1,457$ and $1,510\text{ cm}^{-1}$, corresponding to the disorder mode (D) and the antisymmetric $C_{\alpha}=C_{\beta}$ ring stretching mode (ν_1), respectively [67, 134, 135], were increased, up-shifted, and broadened with increasing E-beam dose. The changes in the D and ν_1 vibration peaks indicate structural modifications to the main polymeric chains in the NW. The spectra reveal that focused E-beam irradiation induces conformational changes in the polymer chains at the nanoscale level and causes a decrease in the doping level of the polymer [67].

Figure 24a shows a schematic diagram of multiple 1D serial junctions of a single P3MT NW on Au electrodes through focused E-beam treatment. The dose of the focused E-beam was fixed to 1.0×10^{17} electrons/cm². Figure 24b shows a comparison of the current–voltage (I – V) characteristic curves of a single pristine P3MT NW and a NW treated with a focused E-beam to form single, double, and triple nanojunctions. As the number of treated sections (i.e., junctions) increased, the current levels of the single P3MT NW decreased dramatically, and the nonlinearity of the I – V curves became severe. The results were similar to those reported for heterojunction nanomaterials with multiple 1D serial sections and superlattice structures [125, 136, 137]. The voltage dependence of the differential conductance in the low-bias region was reduced and sharpened when the number of junctions was increased, as shown in Fig. 24c. The results suggest that the treated sections act as tunneling barriers for charge transport [136, 138].

5.3 Biosensing

An efficient method for DNA detection without a fluorescent dye on the nanoscale can be realized through the use of a single light-emitting polymer NW with lightly doped states, as reported by Park and coworkers [139]. Biological materials can be

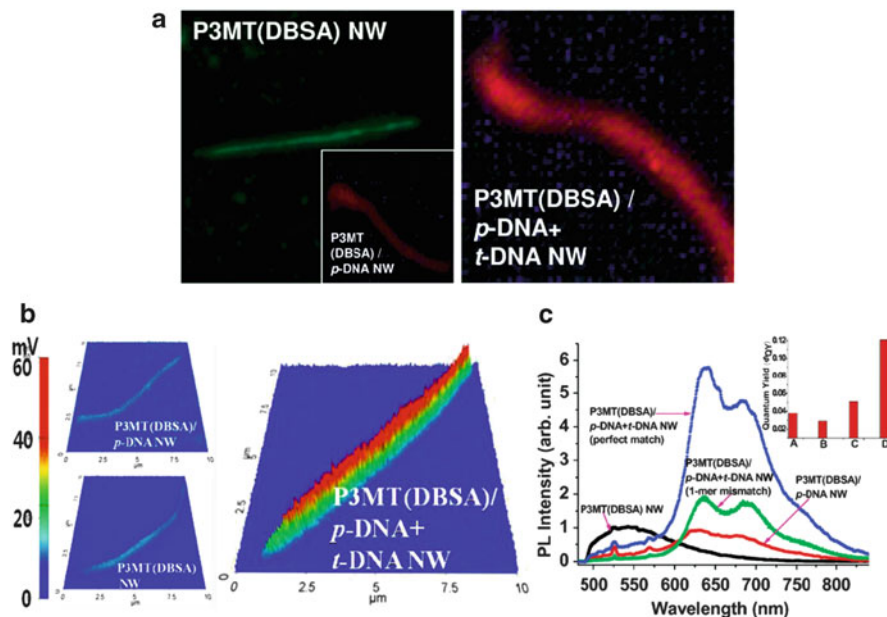


Fig. 25 (a) Color CCD images of P3MT(DBSA) (*left*) and P3MT(DBSA)/*p*-DNA + *t*-DNA (*right*) single NWs. *Inset*: color CCD image of a P3MT(DBSA)/*p*-DNA single NW. (b) 3D LCM PL images of a P3MT(DBSA) (*left top*), P3MT(DBSA)/*p*-DNA (*left bottom*), and P3MT(DBSA)/*p*-DNA + *t*-DNA single NWs (*right*). (c) LCM PL spectra of P3MT(DBSA), P3MT(DBSA)/*p*-DNA, P3MT(DBSA)/*p*-DNA + *t*-DNA (1-mer mismatch), and P3MT(DBSA)/*p*-DNA + *t*-DNA (perfect match) single NWs. *Inset*: quantum yield of P3MT(DBSA) (A), P3MT(DBSA)/*p*-DNA (B), P3MT(DBSA)/*p*-DNA + *t*-DNA (1-mer mismatch) (C), and P3MT(DBSA)/*p*-DNA + *t*-DNA (perfect match) (D) NWs. (Reproduced with permission from [139]. Copyright 2011 Royal Society of Chemistry.)

detected readily through variations in the light-emitting characteristics of the polymer NWs with high signal amplification when the appropriate receptors are linked to the surfaces of the NWs. The light-emitting P3MT material is a promising system to study dopant-mediated DNA detection in fluorescence chain reaction-enhanced PL because of the formation of doping-induced bipolaron (i.e., cationic) states.

Figure 25 shows color CCD images and LCM PL images and spectra of an isolated single P3MT NW with DBSA dopant in the as-prepared, *p*-DNA attached, and *t*-DNA hybridized states. The luminescence color of the single P3MT(DBSA) NW was green with relatively low brightness (left image of Fig. 25a). When coupled with *p*-DNA, the luminescence color changed from green to red (inset of left image of Fig. 25a). This red-shift is attributed to conformational modification of the P3MT main chains by electrostatic interactions between the SO_3^- group of the NW and the NH_3^+ group and the negatively charged phosphate backbone of the wrapping *p*-DNAs. After hybridization with *t*-DNA, the luminescence intensity was enhanced considerably

compared to as-prepared and *p*-DNA-immobilized P3MT(DBSA) NWs, as shown in the right image of Fig. 25a.

Figure 25b shows 3D LCM PL images of the P3MT(DBSA), P3MT(DBSA)/*p*-DNA, and P3MT(DBSA)/*p*-DNA + *t*-DNA single NWs. The average voltages of the LCM PL intensities for the as-prepared P3MT(DBSA), P3MT(DBSA)/*p*-DNA, and P3MT(DBSA)/*p*-DNA + *t*-DNA single NWs were 11 (± 2), 10 (± 1), and 61 (± 3) mV, respectively. The LCM PL intensity of the functionalized P3MT(DBSA)/*p*-DNA + *t*-DNA single NW was about six times higher than that of the as-prepared P3MT(DBSA) single NW.

The LCM PL spectra of the single NWs were compared, as shown in Fig. 25c. The main PL peak of the as-prepared single NW was observed at ~ 554 nm. When coupled with *p*-DNA, the main PL peak was red-shifted to ~ 640 nm and its intensity decreased slightly. Upon hybridization of the P3MT(DBSA)/*p*-DNA NW with *t*-DNA, the maximum intensity of the LCM PL peak was enhanced up to about six times compared with that of the as-prepared NW. The change in the luminescence characteristics of P3MT(DBSA) NWs was also studied using 1-mer mismatched *t*-DNAs. When the *p*-DNAs were coupled with the 1-mer mismatched *t*-DNAs (100 nM), the LCM PL intensity of the P3MT(DBSA)/*p*-DNA + *t*-DNA (1-mer mismatch) single NW was much lower than that in the perfect match case, as shown in Fig. 25c. The significant increase in the PL intensity of the P3MT(DBSA)/*p*-DNA + *t*-DNA single NW might be due to the dopant-mediated energy transfer effect in the fluorescence chain reaction between the *t*-DNA and light-emitting P3MT chains. These results highlight the possibility for nanoscale optical detection of DNA without a fluorescent dye using a light-emitting P3MT(DBSA) single NW on the basis of the change in the luminescence color and intensity.

The nanoscale luminescence characteristics of a single P3MT NW with a different dopant, namely, tetrabutylammonium trifluoromethane sulfuric acid (TBACF₃SO₃), and the DNA-functionalized states were examined to reconfirm the feasibility of dopant-mediated DNA detection. Weak green light emission was observed for the P3MT(TBACF₃SO₃) single NW (left image of Fig. 26a). When the NWs were coupled with *p*-DNA, the color changed from green to red with a slightly decrease in luminescence intensity, as shown in the inset of the left image of Fig. 26a. The luminescence color CCD image of a P3MT(TBACF₃SO₃)/*p*-DNA + *t*-DNA single NW showed significantly brighter red light emission than the single NW without *t*-DNA (right image of Fig. 26a). The novel PL enhancement of P3MT(TBACF₃SO₃) single NWs through hybridization with *t*-DNA was examined as a function of the *t*-DNA concentration from 100 μ M to 100 nM, as shown in Fig. 26b. As the concentration of *t*-DNA increased, the LCM PL intensity of the single NW also increased, suggesting that effective energy transfer occurs in the fluorescence chain reaction between the light-emitting NW and *t*-DNAs. The maximum intensity of the LCM PL peak and its integrated area for a single NW hybridized with complementary *t*-DNA (100 nM) increased by a maximum of approximately 30-fold compared with that of the as-prepared and *p*-DNA-functionalized NWs. In addition, the LCM PL intensity of the NW hybridized with *t*-DNA at a concentration of 100 μ M increased seven to eightfold compared with that of the NW without *t*-DNA.

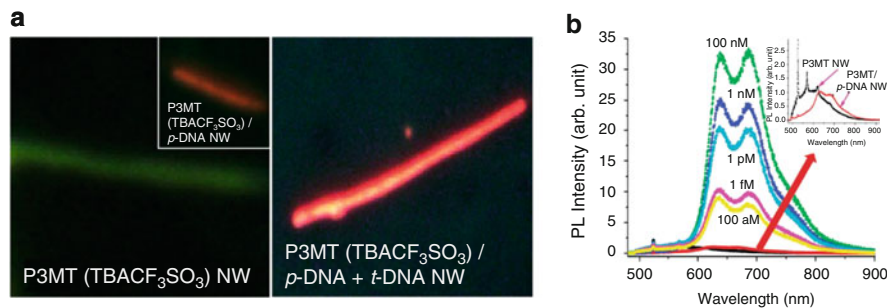


Fig. 26 (a) Color CCD images of P3MT(TBACF₃SO₃) (left) and P3MT(TBACF₃SO₃)/p-DNA + t-DNA (right) single NWs. *Inset*: color CCD image of a P3MT(TBACF₃SO₃)/p-DNA single NW. (b) LCM PL spectra of P3MT(TBACF₃SO₃), P3MT(TBACF₃SO₃)/p-DNA, and P3MT(TBACF₃SO₃)/p-DNA + t-DNA single NWs with various concentrations of t-DNA (from 100 aM to 100 nM). *Inset*: magnification of LCM PL spectra of P3MT(TBACF₃SO₃) and P3MT(TBACF₃SO₃)/p-DNA single NWs. (Reproduced with permission from [139]. Copyright 2011 Royal Society of Chemistry.)

5.4 Nano-optoelectronics

Organic photodiodes and phototransistors are fabricated by using photosensitive π -conjugated organic materials, and the photovoltaic properties of these materials have been intensively studied for application to inexpensive and renewable energy sources [140]. The mechanism of charge recombination and dissociation in the p - n junctions of semiconductors is used in various applications such as diode lasers, LEDs, photodetectors, and photovoltaic cells. With the rapid development of nanotechnology, nanoscale p - n junctions have been investigated by using low-dimensional nanostructures such as carbon nanotubes (CNTs) and inorganic or organic semiconducting NWs.

A doped Si substrate with as-grown multiwalled (MW) CNTs synthesized through a thermal chemical vapor deposition (CVD) method was attached to a stainless steel working electrode, as shown in Fig. 27a [141]. A P3HT layer with a thickness of ~ 20 nm was directly deposited on the surface of the MWCNTs using an electrochemical polymerization method. The electrolyte for the electrochemical polymerization consisted of 3-HT monomers, BMIMPF₆ as the ionic liquid, and anhydrous acetonitrile as the solvent.

The formation and surface morphology of the coaxial P3HT/MWCNT hybrid NTs were investigated using HR-TEM, as shown in Fig. 27b [141]. The MWCNTs had an outer diameter of 10–30 nm and a wall thickness of 2–8 nm. The total diameter of the hybrid NTs was ~ 60 nm. The thickness of the P3HT layer deposited on the MWCNTs was ~ 20 (± 10) nm, and the formation of the coaxial-type MWCNTs coated with P3HT was clearly observed.

Figure 27c shows a schematic illustration of the four-probe electrodes on a P3HT/MWCNT hybrid single NT. Two Au/Ti electrodes make contact with the outer P3HT single NT, while the other two make contact with the inner single

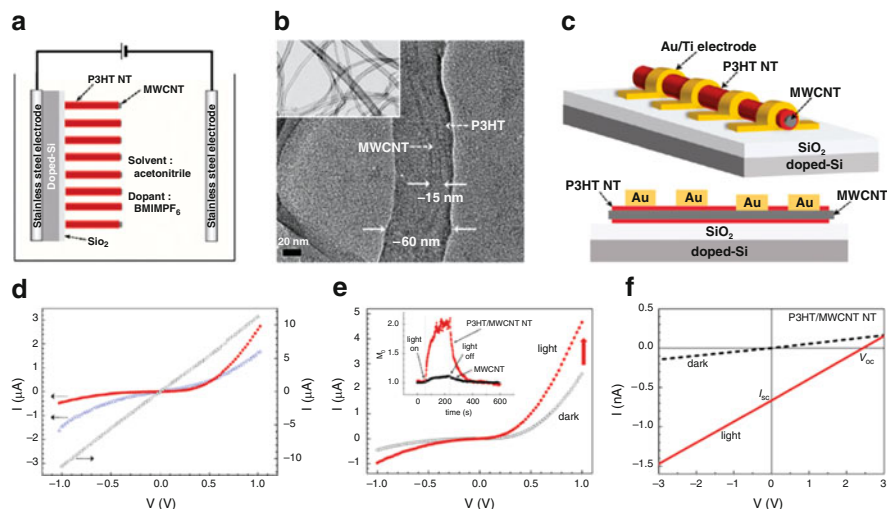


Fig. 27 (a) Illustration of electrochemical deposition of P3HT on the MWCNT surface. (b) HR-TEM image of P3HT/MWCNT hybrid NT. *Inset*: HR-TEM image of MWCNTs. (c) Diagram of single P3HT/MWCNT hybrid NT with four-probe Au/Ti electrodes (*top*) and cross-sectional view of P3HT/MWCNT hybrid NT with electrodes (*bottom*). (d) Comparison of I - V characteristic curves of a single P3HT NT, MWCNT, and P3HT/MWCNT hybrid NT measured in the dark at room temperature. (e) Comparison of I - V characteristic curves of P3HT/MWCNT hybrid NT with and without illumination. *Inset*: comparison of normalized currents of P3HT/MWCNT hybrid NT and MWCNT with and without illumination as a function of time. (f) I - V characteristic curves representing quasi-photovoltaic effect with and without illumination for a single P3HT/MWCNT hybrid NT. (Reproduced with permission from [141]. Copyright 2010 American Chemical Society.)

MWCNT through partial etching of P3HT. Figure 27d shows the I - V characteristic curves of a single NT in the dark at room temperature. The I - V characteristic curve for the outer P3HT single NT in the hybrid NT shows semiconducting behavior, whereas ohmic behavior is observed for the inner single MWCNT, as shown in Fig. 27d. From the slope of the I - V curves for the MWCNT, the conductivity of the single MWCNT was estimated to be 10^3 - 10^4 S/cm. The current level of the P3HT NT is much smaller than that of the MWCNT. When two electrodes were separately contacted with the MWCNT and the P3HT NT, the I - V characteristic curve of the single P3HT/MWCNT hybrid NT showed rectification behavior (i.e., nanorectifier) owing to the formation of a hybrid junction between the MWCNT and the semiconducting P3HT NT.

Figure 27e shows the photoresponsive I - V characteristics of a P3HT/MWCNT hybrid single NT. Under illumination (100 mW/cm^2), the I - V characteristics of the P3HT/MWCNT hybrid NT also show rectification behavior. The current levels of the hybrid single NT were enhanced through the illumination, as shown in Fig. 27e. The increase in the current level of the P3HT/MWCNT hybrid NT through illumination was relatively higher than that of the MWCNT, as shown in the inset of

Fig. 27e. Figure 27f shows the quasi-photovoltaic effect (i.e., the linear increase in the photocurrent with the applied bias) measured in the P3HT/MWCNT hybrid single NT. In the experiments, the short circuit current (I_{sc}) was measured to be -0.67 nA, and the open circuit voltage (V_{oc}) was measured to be 2.44 mV. The power conversion efficiency (η) of the P3HT/MWCNT hybrid single NT was estimated to be $\sim 0.42\%$.

Nanoscale photovoltaic cells are now considered as potentially new types of solar energy harvesting nanosystems. A single coaxial silicon NW with a *p*-type/intrinsic/*n*-type (PIN)-doped semiconductor structure has been experimentally realized as a nanoscale electronic power source [142]. Recently, single NW photovoltaic devices using coaxial NWs consisting of ZnO and P3HT were shown to exhibit a η value of 0.036% [143]. The nanoscale photovoltaic cells using the coaxial NWs, composite NWs, or various nanostructures must be studied to fabricate high-efficiency future energy harvesting systems.

Figure 28a shows the fabrication process for the P3HT:PCBM composite NWs through a wetting method by using Al_2O_3 nanoporous templates with a pore size of 100 nm [144]. Figure 28b shows the normalized LCM PL spectra ($\lambda_{ex} = 488$ nm) for single NWs of P3HT, PCBM, and P3HT:PCBM composite (1:1 wt%). For single P3HT NW, the LCM PL peaks corresponding to the 0–0 and 0–1 transitions of P3HT were observed at 650 and 700 nm, respectively. The LCM PL peak of the single PCBM NW was observed at 730 nm, with a shoulder peak at 810 nm. For the single P3HT:PCBM composite NW, the maximum LCM PL peak was observed at 725 nm, with shoulder peaks at 650 and 810 nm, indicating the coexistence of P3HT and PCBM phases in the single NW.

Figure 28c, d shows a schematic illustration and SEM image of a nanodevice comprising a single P3HT:PCBM NW with Au and Al electrodes. The I – V characteristic curve of the single P3HT:PCBM (1:2 wt%) NW in the dark shows diode-like behavior, as shown in Fig. 28e. Under illumination, the current levels were enhanced at a relatively high bias ($V \geq 10$ V), as shown in Fig. 28e. Excitons were created in the major P3HT and minor PCBM components, and they dissociated into electrons and holes under the applied electric field near the interface between P3HT and PCBM.

Recently, Lee and coworkers reported the fabrication and nanoscale physical properties of hybrid P3HT/PCBM NPs and their photovoltaic applications [52]. Figure 29a shows the LCM PL spectra of annealed and non-annealed hybrid NPs of *p*-type P3HT and *n*-type PCBM prepared by the mini-emulsion method [46, 50]. From the wide-angle X-ray diffraction patterns, the annealed P3HT NPs had a larger crystalline size (~ 76.5 Å) than non-annealed NPs (58.8 Å), as shown in the right inset of Fig. 29a. The LCM PL intensities of single annealed and non-annealed hybrid P3HT/PCBM NPs were lower than those of a single annealed P3HT NP, as shown in Fig. 29a, indicating PL quenching.

Figure 29b shows the scheme of a conducting atomic force microscope (c-AFM) experiment using a single hybrid P3HT/PCBM NP. An indium tin oxide (ITO) electrode was used as the cathode because of its relatively low work function (4.8 eV) compared with that (5.1 eV) of the Pt metal used as the anode. Figure 29c

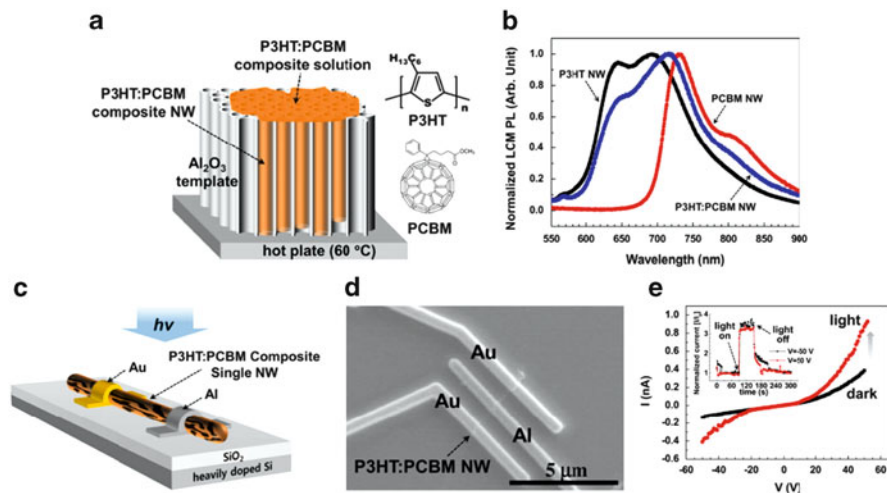


Fig. 28 (a) Fabrication process for P3HT:PCBM composite NWs. (b) Comparison of normalized LCM PL spectra for single NWs of P3HT, PCBM, and P3HT:PCBM composite. (c) Nanodevice with Au and Al electrodes using P3HT:PCBM single NW. (d) SEM image of nanodevice using a single NW with Au and Al electrodes. (e) I - V characteristic curves for single P3HT:PCBM NW with a P3HT:PCBM concentration of 1:2 wt% with and without irradiation. *Inset*: normalized currents of the composite NW with and without illumination as a function of time. (Reproduced with permission from [144]. Copyright 2011 Elsevier B.V.)

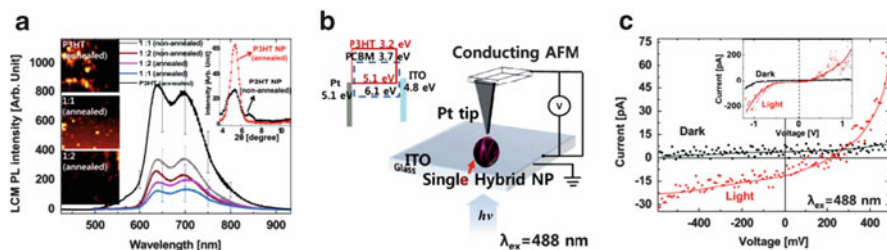


Fig. 29 (a) LCM PL intensities of single annealed P3HT NPs and annealed and non-annealed P3HT/PCBM (1:1 and 1:2 wt%) NPs and hybrid NPs. *Left insets*: LCM PL mapping images of annealed P3HT and hybrid NPs. *Right inset*: wide-angle X-ray diffraction patterns of annealed and non-annealed P3HT NPs. (b) Illustration of c-AFM experiment using single hybrid P3HT/PCBM NP. *Inset*: energy band diagram of hybrid NP with Pt and ITO electrodes. (c) Photovoltaic I - V characteristic curves of single annealed P3HT/PCBM (1:2 wt%) NP. *Inset*: photoresponsive I - V characteristic curves of NPs in the full measured range. The *lines* are guides for the eye. (Reproduced with permission from [52]. Copyright 2012 Royal Society of Chemistry.)

shows the photoresponsive I - V characteristic curves in a low-bias regime for a single annealed P3HT/PCBM (1:2 wt%) NP at room temperature. The photovoltaic effect was observed in the single annealed hybrid NP, as shown in Fig. 29c. From the photovoltaic I - V characteristic curves, the open-circuit voltage and short-circuit current were measured to be about 293.15 mV and 11.29 pA, respectively, and the

fill factor was estimated to be about 0.398. The monochromatic η ($\lambda_{\text{ex}} = 488 \text{ nm}$) of the single annealed P3HT/PCBM (1:2 wt%) NP was estimated to be about $1.32 \times 10^{-5}\%$.

6 Conclusions and Outlooks

Nanostructures of light-emitting polymers with π -conjugated structure have been synthesized and used as electronic and optical nanomaterials for nanoscale optoelectronic devices and biosensors. Various synthetic methods such as chemical, electrochemical, reprecipitation, and electrospinning methods with or without nanoporous templates have been developed for the fabrication of polymer nanostructures. The physical sizes and formation of the nanostructures can be controlled by adjusting the synthetic conditions. High-resolution LCM spectroscopy allowed investigation of the light emission characteristics of individual nanostructures. The light absorption and emission efficiencies of the light-emitting polymer nanostructures can be tuned by chemical processing and post-synthetic treatments, as well as by adjusting their physical dimensions. Post-synthetic treatments such as electrochemical doping, E-beam irradiation, hydrothermal processing, and nanoscale metal hybridization were used to modify the intrinsic properties of the polymer nanostructures. The electronic structures of polymer NTs and NWs can be varied through electrochemical doping and E-beam irradiation. The optical properties and formation of NPs are dependent on the hydrothermal temperature. The hybridization of polymer nanostructures with nanoscale metals induces drastic PL enhancement owing to SPR coupling. The light-emitting polymer nanostructures introduced here can be applied to nanoscale identification barcodes, label-free DNA-sensing, nanodiodes, and nanophotovoltaic devices. Industrial applications of light-emitting polymer nanostructures are in their nascent stages. Homogeneous dispersions of nanomaterials must be developed to enable further applications in flexible optoelectronics. In addition, advanced device fabrication techniques using single nanostructures are also required for nano-optoelectronics.

Acknowledgments This work was partially supported from the National Research Foundation (NRF) grant funded by the Korean government (MEST) (No. 2012R1A2A2A01045102).

References

1. MacDiarmid AG (2001) *Rev Mod Phys* 73:701–712
2. Shirakawa H (2001) *Rev Mod Phys* 73:713–718
3. Heeger AJ (2001) *Rev Mod Phys* 73:681–700
4. Skotheim TA, Elsenbaumer RL, Reynolds JR (1998) *Handbook of conducting polymers*. Dekker, New York
5. Perepichka IF, Perepichka DF, Meng H, Wudl F (2005) *Adv Mater* 17:2281–2305

6. Park DH, Kim MS, Joo J (2010) *Chem Soc Rev* 39:2439–2452
7. Roth S, Carroll DL (2004) *One-dimensional metals*, 2nd edn. Wiley, Weinheim
8. Heeger AJ (2002) *Synth Met* 125:23–42
9. Su WP, Schrieffer JR, Heeger AJ (1979) *Phys Rev Lett* 42:1698–1701
10. Su WP, Schrieffer JR, Heeger AJ (1980) *Phys Rev B* 22:2099–2111
11. Heeger AJ, Kivelson S, Schrieffer JR, Su WP (1988) *Rev Mod Phys* 60:781–850
12. Roothaan CCJ (1951) *Rev Mod Phys* 23:69–89
13. Anderson PW (1975) *Phys Rev Lett* 34:953–955
14. Brédas JL, Chance RR, Baughman RH, Silbey R (1982) *J Chem Phys* 76:3673–3678
15. Brédas JL, Thémans B, André JM (1982) *J Chem Phys* 78:6137–6148
16. Brédas JL, Elsenbaumer RL, Chance RR, Silbey R (1983) *J Chem Phys* 78:5656–5662
17. Brédas JL, Thémans B, André JM (1983) *Phys Rev B* 27:7827–7830
18. Fesser K, Bishop AR, Campbell DK (1983) *Phys Rev B* 27:4804–4825
19. Brédas JL, Scott JC, Yakushi K, Street GB (1984) *Phys Rev B* 30:1023–1025
20. Kaufman JH, Colaneri N, Scott JC, Street GB (1984) *Phys Rev Lett* 53:1005–1008
21. Brédas JL, Street GB (1985) *Acc Chem Res* 18:309–315
22. Vardeny Z, Ehrenfreund E, Brafman O, Nowak M, Schaffer H, Heeger AJ, Wudl F (1986) *Phys Rev Lett* 56:671–674
23. Sum U, Fesser K, Büttner H (1988) *Phys Rev B* 38:6166–6173
24. Sun ZW, Frank AJ (1991) *J Chem Phys* 94:4600–4608
25. Martin CR (1994) *Science* 266:1961–1966
26. Feng S, Xu R (2001) *Acc Chem Res* 34:239–247
27. Joo J, Kim BH, Park DH, Sung JH, Choi HJ (2008) Conducting polymer nanotubes, nanowires, and nanocomposites: synthesis, characteristics, and applications. In: Nalwa HS (ed) *Handbook of organic electronics and photonics*, vol 1. American Scientific, California, pp 51–83
28. Long YZ, Li MM, Gu C, Wan M, Duvail JL, Liu Z, Fan Z (2011) *Prog Polym Sci* 36:1415–1442
29. Jones MR, Osberg KD, MacFarlane RJ, Langille MR, Mirkin CA (2011) *Chem Rev* 111:3736–3827
30. Kim FS, Ren G, Jenekhe SA (2011) *Chem Mater* 23:682–732
31. Joo J, Kim BH, Park DH, Kim HS, Seo DS, Shim JH, Lee SJ, Ryu KS, Kim K, Jin JI, Lee TJ, Lee CJ (2005) *Synth Met* 153:313–316
32. Kim BH, Park DH, Joo J, Yu SG, Lee SH (2005) *Synth Met* 150:279–284
33. Park DH, Kim BH, Jang MK, Bae KY, Lee SJ, Joo J (2005) *Synth Met* 153:341–344
34. Park JG, Lee SH, Kim B, Park YW (2002) *Appl Phys Lett* 81:4625–4627
35. Huang J, Kaner RB (2004) *J Am Chem Soc* 126:851–855
36. Tran HD, Kaner RB (2006) *Chem Commun* 2006:3915–3917
37. Dan LI, Huang J, Kaner RB (2009) *Acc Chem Res* 42:135–145
38. Kim K, Jin JI (2001) *Nano Lett* 1:631–636
39. Sadki S, Schottland P, Brodie N, Sabouraud G (2000) *Chem Soc Rev* 29:283–293
40. Park DH, Kim BH, Jang MG, Bae KY, Joo J (2005) *Appl Phys Lett* 86:113116
41. Park DH, Kim M, Kim MS, Kim DC, Song H, Kim J, Joo J (2008) *Electrochem Solid State Lett* 11:K69–K72
42. Lee SH, Park DH, Kim K, Joo J, Kim DC, Kim HJ, Kim J (2007) *Appl Phys Lett* 91:263102
43. Park DH, Kim HS, Lee YB, Ko JM, Lee JY, Kim HJ, Kim DC, Kim J, Joo J (2008) *Synth Met* 158:90–94
44. Parthasarathy RV, Martin CR (1994) *Chem Mater* 6:1627–1632
45. Horn D, Rieger J (2001) *Angew Chem Int Ed* 40:4330–4361
46. Kasai H, Nalwa HS, Oikawa H, Okada S, Matsuda H, Minami N, Kakuta A, Ono K, Mukoh A, Nakanishi H (1992) *Jpn J Appl Phys* 31:L1132–L1134
47. Kong F, Sun YM, Yuan RK (2007) *Nanotechnology* 18:265707
48. Shimizu H, Yamada M, Wada R, Okabe M (2008) *Polym J* 40:33–36

49. Landfester K, Montenegro R, Scherf U, GüNTNER R, Asawapirom U, Patil S, Neher D, Kietzke T (2002) *Adv Mater* 14:651–655
50. Kietzke T, Neher D, Landfester K, Montenegro R, Güntner R, Scherf U (2003) *Nat Mater* 2:408–412
51. Kim MS, Park DH, Cho EH, Kim KH, Park QH, Song H, Kim DC, Kim J, Joo J (2009) *ACS Nano* 3:1329–1334
52. Lee YB, Lee SH, Kim K, Lee JW, Han KY, Kim J, Joo J (2012) *J Mater Chem* 22:2485–2490
53. Reneker DH, Chun I (1996) *Nanotechnology* 7:216–223
54. Li D, Xia Y (2004) *Adv Mater* 16:1151–1170
55. Greiner A, Wendorff JH (2007) *Angew Chem Int Ed* 46:5670–5703
56. Reneker DH, Yarin AL (2008) *Polymer* 49:2387–2425
57. Lu X, Wang C, Wei Y (2009) *Small* 5:2349–2370
58. Kim JS, Reneker DH (1999) *Polym Eng Sci* 39:849–854
59. Li D, Xia Y (2004) *Nano Lett* 4:933–938
60. Laforgue A (2011) *J Power Sources* 196:559–564
61. Kim HJ, Kim DC, Kim R, Kim J, Park DH, Kim HS, Joo J, Suh YD (2007) *J Appl Phys* 101:053514
62. Hong YK, Park DH, Jo SG, Koo MH, Kim DC, Kim J, Kim JS, Jang SY, Joo J (2011) *Angew Chem Int Ed* 50:3734–3738
63. Kim DC, Kim R, Kim HJ, Kim J, Park DH, Kim HS, Joo J (2007) *Jpn J Appl Phys* 46:5556–5559
64. Joo J, Park DH, Jeong MY, Lee YB, Kim HS, Choi WJ, Park QH, Kim HJ, Kim DC, Kim J (2007) *Adv Mater* 19:2824–2829
65. Park DH, Kim HS, Jeong MY, Lee YB, Kim HJ, Kim DC, Kim J, Joo J (2008) *Adv Funct Mater* 18:2526–2534
66. Yassar A, Roncali J, Garnier F (1989) *Macromolecules* 22:804–809
67. Hong YK, Park DH, Park SK, Song H, Kim DC, Kim J, Han YH, Park OK, Lee BC, Joo J (2009) *Adv Funct Mater* 19:567–572
68. Louarn G, Trznadel M, Buisson JP, Laska J, Pron A, Lapkowski M, Lefrant S (1996) *J Phys Chem* 100:12532–12539
69. Jin S, Xue G (1997) *Macromolecules* 30:5753–5757
70. Brédas JL, Thémans B, Fripiat JG, André JM, Chance RR (1984) *Phys Rev B* 29:6761–6773
71. Li Y, Qian R (1988) *Synth Met* 26:139–151
72. Li Y, Qian R (1993) *Synth Met* 53:149–154
73. Padmanaban G, Ramakrishnan S (2000) *J Am Chem Soc* 122:2244–2251
74. Szymanski C, Wu C, Hooper J, Salazar MA, Perdomo A, Dukes A, McNeill J (2005) *J Phys Chem B* 109:8543–8546
75. Liu C, Kwon YK, Heo J (2008) *Chem Phys Lett* 452:281–284
76. Di Benedetto F, Camposeo A, Pagliara S, Mele E, Persano L, Stabile R, Cingolani R, Pisignano D (2008) *Nat Nanotechnol* 3:614–619
77. Lu W, Fadeev AG, Qi B, Smela E, Mattes BR, Ding J, Spinks GM, Mazurkiewicz J, Zhou D, Wallace GG, MacFarlane DR, Forsyth SA, Forsyth M (2002) *Science* 297:983–987
78. Kim HS, Park DH, Lee YB, Kim DC, Kim HJ, Kim J, Joo J (2007) *Synth Met* 157:910–913
79. Santos MJL, Brolo AG, Girotto EM (2007) *Electrochim Acta* 52:6141–6145
80. Garreau S, Louarn G, Buisson JP, Froyer G, Lefrant S (1999) *Macromolecules* 32:6807–6812
81. Colaneri N, Nowak M, Spiegel D, Hotta S, Heeger AJ (1987) *Phys Rev B* 36:7964–7968
82. Kros A, Van Hövell SWFM, Sommerdijk NAJM, Nolte RJM (2001) *Adv Mater* 13:1555–1557
83. Cho SI, Kwon WJ, Choi SJ, Kim P, Park SA, Kim J, Son SJ, Xiao R, Kim SH, Lee SB (2005) *Adv Mater* 17:171–175
84. Abidian MR, Kim DH, Martin DC (2006) *Adv Mater* 18:405–409
85. Groenendaal L, Jonas F, Freitag D, Pielartzik H, Reynolds JR (2000) *Adv Mater* 12:481–494
86. Hong YK, Park DH, Park SK, Joo J (2008) *J Korean Phys Soc* 53:2627–2631

87. Hong YK, Park DH, Park SH, Park SK, Joo J (2009) *Appl Phys Lett* 94:053111
88. Kiriy N, Jähne E, Adler HJ, Schneider M, Kiriy A, Gorodyska G, Minko S, Jehnichen D, Simon P, Fokin AA, Stamm M (2003) *Nano Lett* 3:707–712
89. Cui CX, Kertesz M (1989) *Phys Rev B* 40:9661–9670
90. Brown PJ, Thomas DS, Köhler A, Wilson JS, Kim JS, Ramsdale CM, Siringhaus H, Friend RH (2003) *Phys Rev B* 67:642031–6420316
91. Yu J, Wang W, Cheng B, Su BL (2009) *J Phys Chem C* 113:6743–6750
92. Zhou Y, Bao Q, Tang LAL, Zhong Y, Loh KP (2009) *Chem Mater* 21:2950–2956
93. Jung JS, Lee JW, Kim K, Cho MY, Jo SG, Joo J (2010) *Chem Mater* 22:2219–2225
94. Lee SH, Lee YB, Park DH, Kim MS, Cho EH, Joo J (2011) *Sci Technol Adv Mater* 12:025002
95. Penn RL, Banfield JF (1999) *Geochim Cosmochim Acta* 63:1549–1557
96. Hotta S, Rughooputh SDDV, Heeger AJ, Wudl F (1987) *Macromolecules* 20:212–215
97. Sundberg M, Inganäs O, Stafström S, Gustafsson G, Sjögren B (1989) *Solid State Commun* 71:435–439
98. Yoshino K, Nakao K, Onoda M (1989) *Jpn J Appl Phys* 28:323–324
99. Hess BC, Kanner GS, Vardeny ZV, Baker GL (1991) *Synth Met* 41:1285–1288
100. Clark J, Silva C, Friend RH, Spano FC (2007) *Phys Rev Lett* 98:206406
101. Barnes WL, Dereux A, Ebbesen TW (2003) *Nature* 424:824–830
102. Hu M, Chen J, Li ZY, Au L, Hartland GV, Li X, Marquez M, Xia Y (2006) *Chem Soc Rev* 35:1084–1094
103. Park DH, Kim MS, Cho EH, Park SH, Song H, Kim DC, Kim J, Joo J (2009) *Electrochem Solid State Lett* 12:K5–K8
104. Park DH, Lee YB, Kim HS, Kim DC, Kim J, Joo J (2009) *Synth Met* 159:22–25
105. Daniel MC, Astruc D (2004) *Chem Rev* 104:293–346
106. Tseng RJ, Huang J, Ouyang J, Kaner RB, Yang Y (2005) *Nano Lett* 5:1077–1080
107. Quinn BM, Dekker C, Lemay SG (2005) *J Am Chem Soc* 127:6146–6147
108. Wildgoose GG, Banks CE, Compton RG (2006) *Small* 2:182–193
109. Dong SK, Lee T, Geckeler KE (2006) *Angew Chem Int Ed* 45:104–107
110. Zhu J, Brink M, McEuen PL (2008) *Nano Lett* 8:2399–2404
111. Chiu NF, Lin CW, Lee JH, Kuan CH, Wu KC, Lee CK (2007) *Appl Phys Lett* 91:083114
112. Anker JN, Hall WP, Lyandres O, Shah NC, Zhao J, Van Duyne RP (2008) *Nat Mater* 7:442–453
113. Kim SS, Na SI, Jo J, Kim DY, Nah YC (2008) *Appl Phys Lett* 93:073307
114. Park DH, Hong YK, Kim MS, Cho EH, Choi WJ, Kim KH, Park QH, Kim DC, Song H, Kim J, Joo J (2010) *Synth Met* 160:604–608
115. Schuck PJ, Fromm DP, Sundaramurthy A, Kino GS, Moerner WE (2005) *Phys Rev Lett* 94:017402
116. Genet C, Ebbesen T (2007) *Nature* 445:39–46
117. Lassiter JB, Aizpurua J, Hernandez LI, Brandl DW, Romero I, Lal S, Hafner JH, Nordlander P, Hales NR (2008) *Nano Lett* 8:1212–1218
118. Nicewarner-Peña SR, Freeman RG, Reiss BD, He L, Peña DJ, Walton ID, Cromer R, Keating CD, Natan MJ (2001) *Science* 294:137–141
119. Gudiksen MS, Lauthon LJ, Wang J, Smith DC, Lieber CM (2002) *Nature* 415:617–620
120. Tsu R (2005) *Superlattice to nanoelectronics*. Elsevier, Amsterdam
121. Williams BS (2007) *Nat Photonics* 1:517–525
122. Qin L, Banholzer MJ, Millstone JE, Mirkin CA (2007) *Nano Lett* 7:3849–3853
123. Yan R, Gargas D, Yang P (2009) *Nat Photonics* 3:569–576
124. Wade A, Fedorov G, Smirnov D, Kumar S, Williams BS, Hu Q, Reno JL (2009) *Nat Photonics* 3:41–45
125. Björ MT, Ohlsson BJ, Sass T, Persson AI, Thelander C, Magnusson MH, Deppert K, Wallenberg LR, Samuelson L (2002) *Nano Lett* 2:87–89
126. Choi JR, Oh SJ, Ju H, Cheon J (2005) *Nano Lett* 5:2179–2183

127. Lee JH, Wu JH, Liu HL, Cho JU, Cho MK, An BH, Min JH, Noh SJ, Kim YK (2007) *Angew Chem Int Ed* 46:3663–3667
128. Algra RE, Verheijen MA, Borgström MT, Feiner LF, Immink G, Van Enckevort WJP, Vlieg E, Bakkers EPAM (2008) *Nature* 456:369–372
129. Bulbarello A, Sattayasamitsathit S, Crevillen AG, Burdick J, Mannino S, Kanatharana P, Thavarungkul P, Escarpa A, Wang J (2008) *Small* 4:597–600
130. Caroff P, Dick KA, Johansson J, Messing ME, Deppert K, Samuelson L (2009) *Nat Nanotechnol* 4:50–55
131. Park DH, Hong YK, Cho EH, Kim MS, Kim DC, Bang J, Kim J, Joo J (2010) *ACS Nano* 4:5155–5162
132. Krasheninnikov AV, Banhart F (2007) *Nat Mater* 6:723–733
133. Krasheninnikov AV, Nordlund K (2010) *J Appl Phys* 107:071301
134. Shi G, Xu J, Fu M (2002) *J Phys Chem B* 106:288–292
135. Chen F, Shi G, Zhang J, Fu M (2003) *Thin Solid Films* 424:283–290
136. Devoret MH, Grabert H (1992) *Single charge tunneling: coulomb blockade phenomena in nanostructures*. Plenum, New York
137. Delsing P, Claeson T, Likharev KK, Kuzmin LS (1990) *Phys Rev B* 42:7439–7449
138. Aleshin AN, Lee HJ, Jhang SH, Kim HS, Akagi K, Park YW (2005) *Phys Rev B* 72:1532021–1532024
139. Park DH, Kim N, Cui C, Hong YK, Kim MS, Yang DH, Kim DC, Lee H, Kim J, Ahn DJ, Joo J (2011) *Chem Commun* 47:7944–7946
140. Facchetti A (2011) *Chem Mater* 23:733–758
141. Kim K, Shin JW, Lee YB, Cho MY, Lee SH, Park DH, Jang DK, Lee CJ, Joo J (2010) *ACS Nano* 4:4197–4205
142. Tian B, Zheng X, Kempa TJ, Fang Y, Yu N, Yu G, Huang J, Lieber CM (2007) *Nature* 449:885–889
143. Briseno AL, Holcombe TW, Boukai AI, Garnett EC, Shelton SW, Fréchet JJM, Yang P (2010) *Nano Lett* 10:334–340
144. Kim K, Lee JW, Lee SH, Lee YB, Cho EH, Noh HS, Jo SG, Joo J (2011) *Org Electron* 12:1695–1700